The influence of advertisement boards, street and source layouts on CO dispersion and building intake fraction in three-dimensional urban-like models

To be resubmitted to Building and Environment 2019

The influence of advertisement boards, street and source layouts on CO dispersion and building intake fraction in three-dimensional urban-like models

Yuanyuan Lin[1,2], Guanwen Chen[1,2], Taihan Chen[1,2], Zhiwen Luo[3], Chao Yuan[4], Peng Gao[1,2*], Jian Hang[1,2*]

[1]School of Atmospheric Sciences, Sun Yat-sen University, Guangzhou, P.R. China

[2]Guangdong Province Key Laboratory for Climate Change and Natural Disaster Studies, Sun Yat-sen University, Guangzhou, P.R. China

[3]School of the Built Environment, University of Reading, UK

[4]School of Design and Environment, National University of Singapore, Singapore

*Corresponding author: Peng Gao, Jian Hang

E-mail address: gaopeng8@mail.sysu.edu.cn; hangj3@mail.sysu.edu.cn

Abstract

Heavy traffic flows commonly result in large vehicular pollutant exposure in near-road buildings. Street layouts and pollutant source settings are key factors. Advertisement boards are sometimes adopted for business purpose, but their impacts on pollutant dispersion and exposure are still unclear. Thus, this paper numerically investigates the influence of aspect ratios (building height/street width, H/Ws=1 or 2;

H=30m), source locations and advertisement-board settings on the flow, carbon monoxide (CO) dispersion and exposure within three-dimensional urban-like models under the parallel approaching wind to the main streets. Personal intake fraction (*P_iF*) represents the fraction of total vehicular emissions inhaled averagely by each person of a population. Spatial mean *P_iF* is named as <*P_iF*> and that for the entire building as building intake fraction ($<P\_iF>_B$).

With span-wise CO source fixed in target secondary streets of No 2 or 13 (S2 or S13), <*P_iF*> is particularly large in target streets. $<P\_iF>_B$ decreases exponentially toward downstream from the target street and S13 cases attain greater $<P\_iF>_B$ and larger exponential decreasing rates. Cases with *H*/*Ws*=2 experiences more limited upward dispersion and subsequently smaller <*P_iF*> (0.155-0.339ppm) of entire target street than cases with *H*/*Ws*=1 (0.375-0.731ppm). For cases with stream-wise CO source along the main street (Smain), $<P\_iF>_B$ first rises quickly toward downstream, then adjusts to equilibrium values (0.051-0.063ppm). Finally, with span-wise source, vertical and double-layer advertisement boards produce stronger upward CO transportation and greater $<P\_iF>_B$ than lateral and single-layer types, while with Smain source, the double-layer and lateral types produce larger $<P\_iF>_B$ and shorter exposure adjustment distance.

Key words: Building intake fraction ($<P\_iF>_B$); personal intake fraction (*P_iF*); street aspect ratio (*H*/*W*); advertisement board; CO source location; computational fluid dynamic (CFD) simulation

1 Introduction

Due to the ongoing urbanization worldwide, traffic pollutant emissions have become one of the main pollutant sources in cites [1]. Urban air pollution, as one of the most significant environmental problems, is producing adverse health impacts on city dwellers [2-5]. Heavy traffic flows in the main roads, unfavorable urban layouts and atmospheric conditions commonly result in large vehicular pollutant exposure and high health risk for urban residents.

The flow and pollutant dispersion in urban area are commonly categorized into three length scales, i.e. street-scale (~100m), neighborhood-scale (~1km) and city-scale (~10km), and regional-scale (~100-1000km) [11-13]. Besides reducing regional-scale air pollution [14-15] and lowering vehicular pollutant emissions in local streets, neighborhoods or cities, sustainable urban layout designs are helpful for improving urban ventilation capacity and urban air quality [6-13, 16-20]. As reviewed by the literature [11-13, 16-20], the flow and pollutant dispersion in two-dimensional (2D) street canyon or three-dimensional (3D) urban models have been widely studied by conducting computational fluid dynamic (CFD) simulations, controlled laboratory experiments and full-scale outdoor field measurements. Atmospheric conditions and urban layouts are key parameters to influence the flow, ventilation performance and pollutant dispersion capacity [6-13, 16-20, 22-54]. The important parameters have been investigated such as overall urban form and ambient wind directions[21-25], street aspect ratios [8-10,26-27] and building packing densities [28-32], building height variations [32-34], lift-up building design[35-37], viaduct settings [9-10, 38],

67 urban tree planting [39-41] and vehicle-motion-induced turbulence [42] etc. In
68 addition, atmospheric stabilities and buoyancy force induced by wall heating and solar
69 shading also play a significant role on the flow and urban ventilation if wind speed is
70 relatively small and Richardson number is relatively large [43-54]. Most studies so far
71 mainly investigated turbulent flow characteristics, urban ventilation capacity and
72 spatial distribution of pollutant concentration in various sites of street canyons and at
73 the pedestrian level [16-54].

74 In addition, advertisement-board settings are usually fixed near building wall
75 surfaces in many Asian cities for business purpose. However, the advertisement
76 boards possibly reduce urban wind speed and weaken pollutant dilution capacity. But
77 their impacts on the flow and pollutant exposure in urban districts are still not clear
78 and have been rarely investigated so far. In particular, on average, people spend about
79 90% of their time indoor. Outdoor vehicular air pollutants may penetrate into indoor
80 via doors/windows/leakages/ventilation systems and produce indoor exposure
81 originated from outdoor pollutants [2-5]. Such pollutant exposure to urban residents in
82 near-road buildings commonly experience higher health risks than other kinds of
83 urban micro-environments, which should be paid more concern [6-10]. The impacts
84 of advertisement-board settings integrating with typical urban layouts and pollutant
85 source settings on vehicular pollutant exposure to urban residents in near-road
86 buildings and its surrounding streets should be further quantified.

87 In recent studies, various indexes have been adopted to quantify human exposure
88 of a population exposed to urban air pollutants, including daily pollutant exposure (E_t),

89 intake fraction (*iF*) and health risk (*HR*). Ng and Chau [6] analyzed daily carbon
90 monoxide (CO) E_t concerning the impacts of street setbacks and building permeability
91 on in idealized street canyons by CFD simulations. Kalaiarasan et al. [55] employed
92 *HR* to evaluate the potential health hazard level of traffic-generated PM2.5 at housing
93 buildings located near a major expressway in Singapore. Vehicular *iF* represents the
94 ratio of pollutants inhaled by an exposed population to the total pollutant emissions
95 induced by vehicles. An intake fraction of 1ppm (part per million or 10^{-6}) means
96 inhalation of 1mg of air pollutants with 1kg pollutants being released. For example,
97 street-scale *iF*s were evaluated as 3000ppm in a typical street canyon in midtown
98 Manhattan [7] and 371ppm in a street of central Athens Greece [8]. All these three
99 indexes take age distributions of population, breathing rate, activity patterns in
100 different micro-environments and pollutant concentration into account. However,
101 differing from the other two indexes, the intake fraction *iF* is normalized by the total
102 pollutant mass emission and subsequently independent of different pollutant source
103 release rate, which makes it possible to quantify the impacts of urban layouts and
104 atmospheric conditions etc on pollutant dilution capacity and the related exposure
105 [7-10, 37-38]. For instance, by performing CFD simulations validated and estimated
106 by wind tunnel data, Hang et al. [9] reported street-scale *iF*s of 230-913ppm in 2D
107 shallow street canyons (H/W=0.5-1) with only one main vortex, then He et al. [10]
108 further verified street-scale *iF*s in order of 10^5ppm in 2D high-rise deep street canyons
109 (H/W=5-6) with two main vortexes.

110 Because street-scale *iFs* increase linearly if the population size and density in

111 local streets rise, personal intake fraction (P_iF) was introduced to emphasize the
112 impacts of urban layouts and atmospheric conditions on pollutant exposure for each
113 person on average which is independent of population density and size [9-10]. In
114 particular, Hang et al. [9] estimated spatial mean values of P_iF in entire streets (i.e.
115 $<P\_iF>$) in shallow 2D street canyon (~1-5ppm, H/W=0.5-1), later $<P\_iF>$ in 2D
116 deep street canyons (H/W=5-6) was evaluated (~100-1000ppm) [10]. Then $<P\_iF>$ in
117 3D urban district models were verified one order smaller (~0.1ppm) than 2D street
118 canyon models with similar aspect ratios (H/W=0.5-1) [37-38]. In addition, the
119 literature on 2D street canyon models reported that [51], pollutant concentration
120 decreases exponentially toward downstream street canyons of the target street with
121 traffic carbon monoxide (CO) or particle sources , but such decay processes in 3D
122 urban districts still require further investigations.

123 Therefore, the main purpose of this paper is to quantify the integrating impacts of
124 advertisement boards, span-wise and stream-wise CO source settings and street aspect
125 ratios on pollutant exposure in the target street of typical 3D urban districts and the
126 CO exposure decay processes toward downstream streets. Ambient wind directions
127 also significantly influence pollutant dispersion processes [21-25, 31, 37]. Since the
128 parallel approaching wind direction was reported to attain better urban ventilation
129 capacity than oblique wind directions [21, 23, 31, 37], as a start, this paper first
130 considers the approaching wind parallel to the main streets and perpendicular to the
131 secondary streets. In particular, the overall spatial mean P_iF at all floors in each
132 building (i.e. building intake fraction $<P\_iF>_B$) will be quantified as a key index of

pollutant exposure analysis.

2 Pollutant exposure indexes

To quantify vehicular pollutant exposure, intake fraction (*iF*) is defined in Eq. (1):

$$iF = \sum_{i}^{N}\sum_{j}^{M} P_i \times Br_{i,j} \times \Delta t_{i,j} \times Ce_j \Big/ \dot{m} \quad (1)$$

where P_i denotes the number of population in the i^{th} of total age group (N=3) , $Br_{i,j}$ is the average breathing rate (m^3/s) for one person of the i^{th} age group in the j^{th} micro-environment (M=4), similarly $\Delta t_{i,j}$ is the duration of stay in the j^{th} micro-environment (s) for i^{th} age group, Ce_j means the time-averaged pollutant concentration (kg/m^3) in the j^{th} micro-environment originated from the total vehicular emission (kg). The definition formula (Eq. (1)) also indicates that *iF* is independent on the pollutant source strength, but dependent on the population size and density.

In this study, according to the literature [56], the whole population is divided into three age groups (M=3, Fig.1a): Elders (15.5%), Children (21.2%), and Adults (63.3%). Besides, four micro-environments (N=4) are defined as indoors at home (j=1), other indoor locations (j=2), near vehicles (j=3) and other outdoor locations (j=4) (Fig.1b) [57], among which only indoors at home (j=1) is considered here assuming that present building models are residential type. Activity time pattern and breathing rate in every micro-environment vary for different age groups. Breathing rate for each age group only for indoor at home (j=1) is adopted [58] (Table 1).

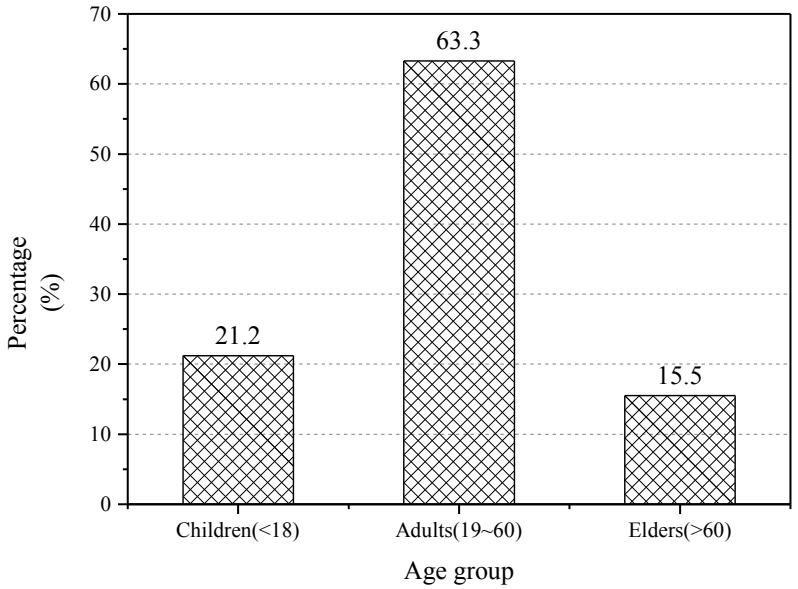

(a)

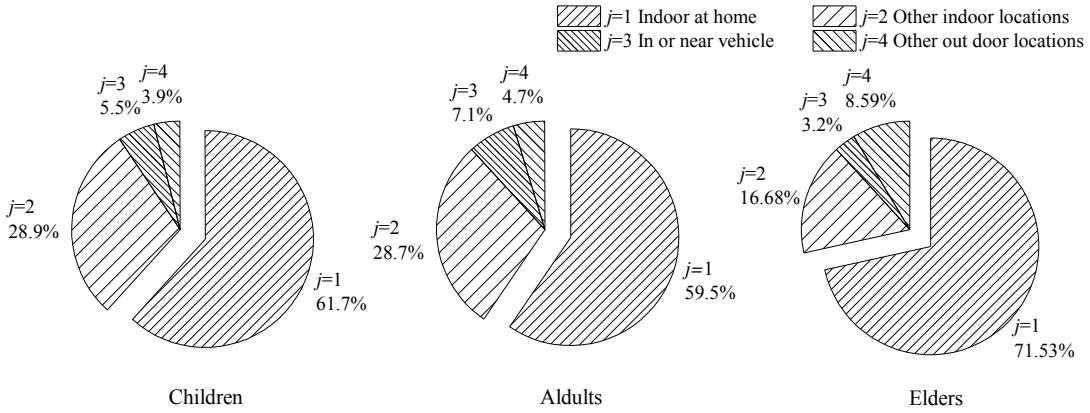

(b)

Fig.1 (a) Age distributions according to the population census in Hong Kong [56]. (b) Time activity patterns for each age group in various micro-environments [57].

Table 1 Breathing rate and time patterns for indoor at home for each age group [58]

Age groups	Population ratio	Breathing rate Br (m^3/day)	Time patterns
Children	21.2%	12.5	61.7%
Adults	63.3%	13.8	59.5%
Elderly	15.5%	13.1	71.6%

163 To obtain an exposure index independent of population density and size, personal
164 intake fraction (*P_iF*) is defined as below [9-10]:

165 $$P\_iF = iF / \sum_{j}^{M} P_i \quad (2)$$

166 *P_iF* represents the averaged pollutant exposure for a population (i.e. intake fraction
167 for each person on average), and does not rise if the population density and size
168 increases. Such index is mainly influenced by multiple factors including urban-built
169 layouts, pollutant source settings, meteorological conditions, time activity patterns for
170 local population etc. [9-10].

171 According to the literature [2-5, 59], if the building is naturally-ventilated, indoor
172 pollutant concentration originated from outdoor pollutants is nearly equal to the
173 outdoor concentration near building surfaces. Therefore, this paper supposes present
174 building models are naturally-ventilated residential type and calculates *P_iFs* at
175 building wall surfaces for each floor as *P_iFs* of rooms inside buildings originated
176 from outdoor traffic emissions. Thus indoor space of buildings is not simulated to
177 reduce the grid number and computational time. The overall spatial mean *P_iF* of all
178 floors of each building is defined as building intake fraction, $\langle P\_iF \rangle_B$.

179

180 ## 3 CFD setups and case descriptions

181 ### 3.1 Numerical models

182 Reynolds-Averaged Navier-Stokes (RANS) approaches (e.g. *k-ε* models and
183 Reynolds stress models (RSM)) are most commonly adopted to predict the flow and
184 turbulence as pollutant dispersion in urban models, although large eddy simulations

(LES) have been confirmed to have higher accuracy while they need much more computing resources and it is a challenge to set appropriate time-dependent inlet boundary conditions. Among the RANS models, it was reported that [16, 60], the standard k-ε model performs worse in predicting turbulence in the strong-wind region of building clusters (e.g flow separation region near building corners) than the modified k-ε models (e.g. RNG k-ε model), but its prediction accuracy is better in simulating weak-wind regions of urban districts (e.g. the sheltered region behind the buildings). In addition, many previous studies confirmed that the standard k-ε model can make satisfactory performance in predicting the flow/pollutant dispersion in urban models and has been validated well by experimental data [9-10, 22-24, 29-33, 42-45].

Therefore, in spite of its limitation in over-predicting the turbulence in urban flow-separation regions, this paper adopted Ansys FLUENT with the standard k-ε model and standard wall function [61] to simulate steady-state flows in full-scale urban models under neutral atmospheric conditions. The governing equations for the flow and turbulent quantities are as below:

The mass conservation equation

$$\frac{\partial \bar{u}_i}{\partial x_i} = 0 \tag{3}$$

The momentum equation

$$\bar{u}_j \frac{\partial \bar{u}_i}{\partial x_i} = -\frac{1}{\rho}\frac{\partial \bar{p}}{\partial x_i} + \frac{\partial}{\partial x_j}\left(\nu \frac{\partial \bar{u}_i}{\partial x_j} - \overline{u_i' u_j'}\right) \tag{4}$$

The transport equations of turbulent kinetic energy (TKE, k) and its dissipation rate (ε):

$$\bar{u}_i \frac{\partial k}{\partial x_i} = \frac{\partial}{\partial x_i}\left[\left(\nu + \frac{\nu_t}{\sigma_k}\right)\frac{\partial k}{\partial x_i}\right] + \frac{1}{\rho}P_k - \varepsilon \tag{5}$$

$$\bar{u}_i \frac{\partial \varepsilon}{\partial x_i} = \frac{\partial}{\partial x_i}\left[\left(\nu + \frac{\nu_t}{\sigma_\varepsilon}\right)\frac{\partial \varepsilon}{\partial x_i}\right] + \frac{1}{\rho}C_{\varepsilon 1}\frac{\varepsilon}{k}P_k - C_{\varepsilon 2}\frac{\varepsilon^2}{k} \tag{6}$$

where $\bar{u}_j$ is time-averaged velocity components ($\bar{u}_j = \bar{u}, \bar{v}, \bar{w}$ j=1, 2, 3), ν and $\nu_t = C_\mu k^2/\varepsilon$ (C_μ=0.09) denote the kinematic viscosity and the kinematic eddy viscosity, $-\overline{u_i' u_j'}$ is the Reynolds stress tensor defined as:

$$-\overline{u_i' u_j'} = \nu_t\left(\frac{\partial \bar{u}_i}{\partial x_j} + \frac{\partial \bar{u}_j}{\partial x_i}\right) - \frac{2}{3}k\delta_{ij} \tag{7}$$

P_k is the turbulence production term defined as:

$$P_k = \nu_t \times \frac{\partial \bar{u}_i}{\partial x_j}\left(\frac{\partial \bar{u}_i}{\partial x_j} + \frac{\partial \bar{u}_j}{\partial x_i}\right) \tag{8}$$

and δ_{ij} is the Kronecker delta whose value is 1 when i=j and 0 otherwise.

All the governing equations (Eqs.(3-6)) were discretized by a finite volume method (FVM) with the second order upwind scheme. The SIMPLE scheme was used for the coupling of pressure and velocity. The under-relaxation factors for pressure term, momentum term, k and ε terms were set as 0.3, 0.7, 0.8 and 0.8 respectively. The simulation stopped until all residuals approximately became constants, and the residuals for typical variables for all cases were under 10^{-6}.

Species transport model was enabled to calculate the dispersion of carbon monoxide (CO) which was used to represent the vehicular emission in this paper. The governing equation of CO concentration is:

$$\bar{u}_j \frac{\partial C}{\partial x_j} - \frac{\partial}{\partial x_j}((D_m + D_t)\frac{\partial C}{\partial x_j}) = S \tag{9}$$

where C is the time-averaged CO concentration (kg/m^3), D_m and D_t are the molecular and turbulent diffusivity respectively, $\overline{u}_j$ is the time-average velocity components in the stream-wise, span-wise and vertical directions ($\overline{u}_j = \overline{u}, \overline{v}, \overline{w}$ when j=1,2,3) and S is the volumetric pollutant emission rate. Here $D_t = \nu_t / Sc_t$ (ν_t is the kinematic eddy viscosity for momentum transport) and Sc_t is the turbulent Schmidt number set as 0.7 according to the literature [21-23, 29-33, 35-38].

The solution of concentration field (Eq.(9)) was discretized by the second-order upwind scheme. Zero normal flux condition was set at all wall surfaces, and zero normal gradient condition was defined at the domain outlet and domain top. The concentration at the domain inlet was set as zero so that there was no additional species injected into the calculation domain except the volumetric CO source defined in the target street. Numerical simulations of Eq.(9) did not stop until its absolute residual became constant and fell below 1×10^{-8}.

3.2 Model descriptions for case studies

Building geometrical setups and CFD settings in flow simulation

As shown in Fig.2a, case studies were based on the idealized 3D urban area with regularly-aligned cubic building models (H=B=30m), with the scale ratio of 200:1 to those in wind tunnel experiments (H=B=15cm) [62]. The approaching wind was parallel to the main streets and perpendicular to the secondary streets. To better illustrate CFD models, it is necessary to mention that, x, y and z represents the stream-wise, span-wise and vertical directions respectively. x/H=0 denotes the

location of windward street opening and y/H=0 represents the vertical symmetric plane of the middle main street. The width of the main street (along x direction, parallel to the approaching wind) is constant as Wm=30m, while the width of secondary streets (along y direction, perpendicular to the approaching wind) changes for different cases (Ws=30m or 15m as H/Ws=1 or 2, Fig.2b-2c).

In order to control the grid number and reduce computing resources, only half of one building column and the main street beside are considered in CFD simulations, and symmetry condition is used for two lateral boundaries of the computational domain (Fig.2b-2d). CFD methodologies with this "half column method" have been confirmed effective by experimental data when the lateral width of urban models is sufficiently large and the airflow is hardly influenced by lateral urban boundaries [32-33, 37, 53, 62-65]. Moreover, under the high-quality CFD validation study, our recent published paper (Hang et al. [38]) also investigated similar urban models by this "half column method".

In addition, distances between urban boundaries and the domain top, domain inlet, domain outlet are not less than 9H, 6.7H and 30H respectively (Fig.2b-2c). At the domain outlet, zero normal gradient boundary condition (i.e. outflow) was set. At the domain top, the symmetry boundary condition was set.

The power-law time-averaged velocity profile $U_0(z)$ measured in the upstream free flow of wind tunnel tests [62] is adopted (Eq.(10)) at the domain inlet. Vertical profiles of $k(z)$ and $\varepsilon(z)$ are calculated by Eq. (11-12) [33, 37, 62-65].

$$U_0(z) = U_{ref} \times (z/H)^{0.16} \tag{10}$$

$$k(z) = u_*^2 / \sqrt{C_\mu} \tag{11}$$

$$\varepsilon(z) = C_\mu^{3/4} k^{3/2} / (\kappa_v z) \tag{12}$$

Here, U_{ref} is the reference velocity magnitude of the approaching free flow at building height (z=H) of wind tunnel models [62] (U_{ref}=3m/s) and u_* is the friction velocity (u_*=0.24m/s) which is the same with that in wind tunnel experiments. C_μ is constant as 0.09 and κ_v is von Karman's constant (κ_v=0.41). Velocity profiles of Eq. (10) at the domain inlet has been adopted in previous CFD studies [23, 33, 37-38, 62-65] which represents a neutral atmospheric boundary layer with a full-scale surface roughness z_0=0.1m and flowing above open rural area with a regular cover of low crop [66]. Vertical profiles of turbulent quantities in Eq.(11-12) were adopted following the CFD guideline [67-68].

Fig.2d illustrates the grid arrangement of base case (Case [None, 30m]). The minimum grid size of 0.2m next to the wall surfaces and a grid expansion ratio of 1.15 were adopted. As verified in Section 4, such grid setup is sufficient to satisfy grid independence requirement (three kinds of grids tested). For all cases studied, the total number of hexahedral cells ranges from 2.8 million to 6.5 million.

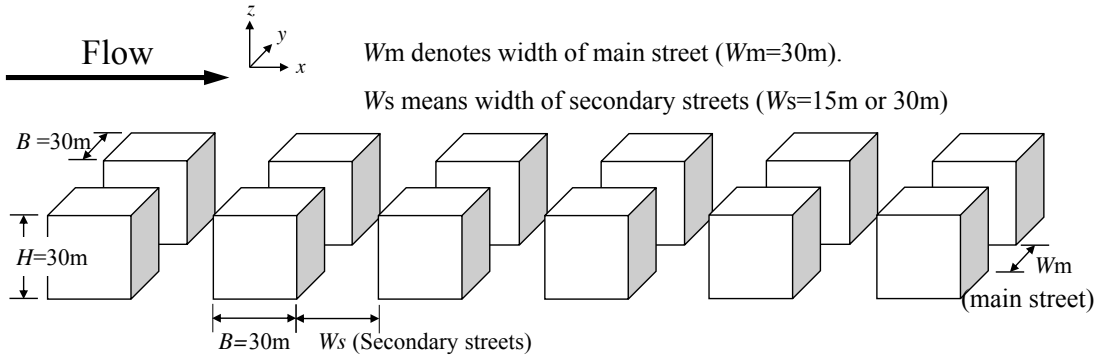

(a)

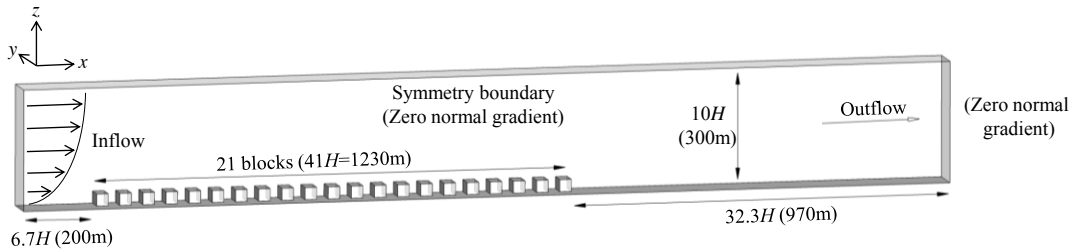

(b)

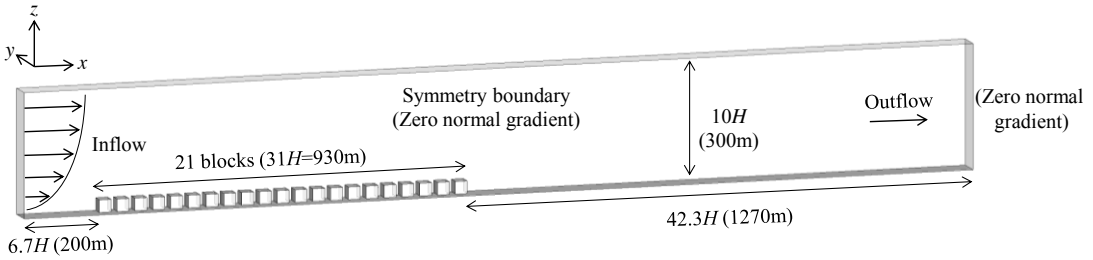

(c)

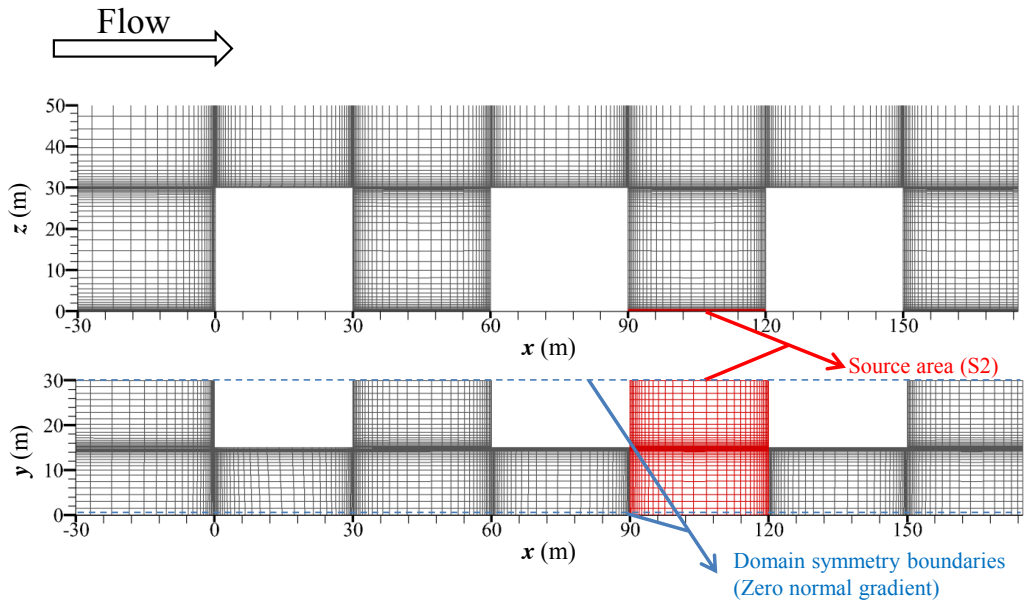

(d)

Fig.2 (a) Idealized urban model; (b-c) Computational domain for cases with *H*/*Ws*=1 and *H*/*Ws*=2; (d) Grid arrangement for cases with aspect ratio *H*/*Ws*=2.

Overall, all CFD setups in case studies, including computational domain size, boundary conditions, grid arrangements etc, satisfy the requirements of CFD guideline for urban wind simulation [67-68]. In particular, numerical accuracy of

present CFD setups has been evaluated well by the CFD validation study in Section 4.

CFD setups in pollutant dispersion simulation

Differing from those of gaseous pollutants, the particle dispersion dynamics also depends on the gravity force and deposition effects associated with particle diameters, dynamic wind, thermal buoyancy forces etc [38, 51]. To simplify the exposure analysis, as a start, this paper mainly emphasizes the dynamic dispersion of passive and gaseous pollutants with inert chemical nature. Similar with the literature [6-10, 37-40, 51], carbon monoxide (CO) was selected as the passive and inert vehicle-emitted pollutants. Two kinds of CO source settings were considered (Fig.3), i.e. a span-wise CO source in the 2nd or 13th secondary streets (S2 in Fig. 3a-3b or S13 in Fig.3c-3d), and the stream-wise CO source along the main street (Smain in Fig.3e-3f). All volume CO sources were set with 0.4m high near street ground (i.e. z_s=0-0.4m). Moreover, span-wise CO sources of S2 and S13 (Fig.3a-3d) had constant span-wise length of S_y=30m in y direction, and the varying stream-wise length in x direction (S_x=Ws=15m or 30m for cases with 30m-wide or 15m-wide secondary streets). In addition, stream-wise CO source (Fig.3e-3f, Smain) was defined as S_y=15m wide in y direction, and in x direction as long as the total stream-wise length of entire urban models (i.e. S_x=L_{x1}=1230m long for 30m-wide cases and S_x=L_{x2}=930m for 15m-wide cases). All pollutant sources were set with a constant CO emission rate of 36.1g/h/m for unit length according to Ng and Chau [6], which was calculated by counting the passing vehicles of a real street per hour in Mongkok, Hong Kong. Thus the total mass emission rate can be defined as $L_{source}\times1.0\times10^{-5}$kg/s, in which L_{source}

differs for different cases: for cases with span-wise CO source (S2 and S13) L_{source}=L_y=30m, for cases with stream-wise CO source (Smain) L_{source}=L_{x1}=1230m or 930m (i.e. equal to total stream-wise length of entire urban model).

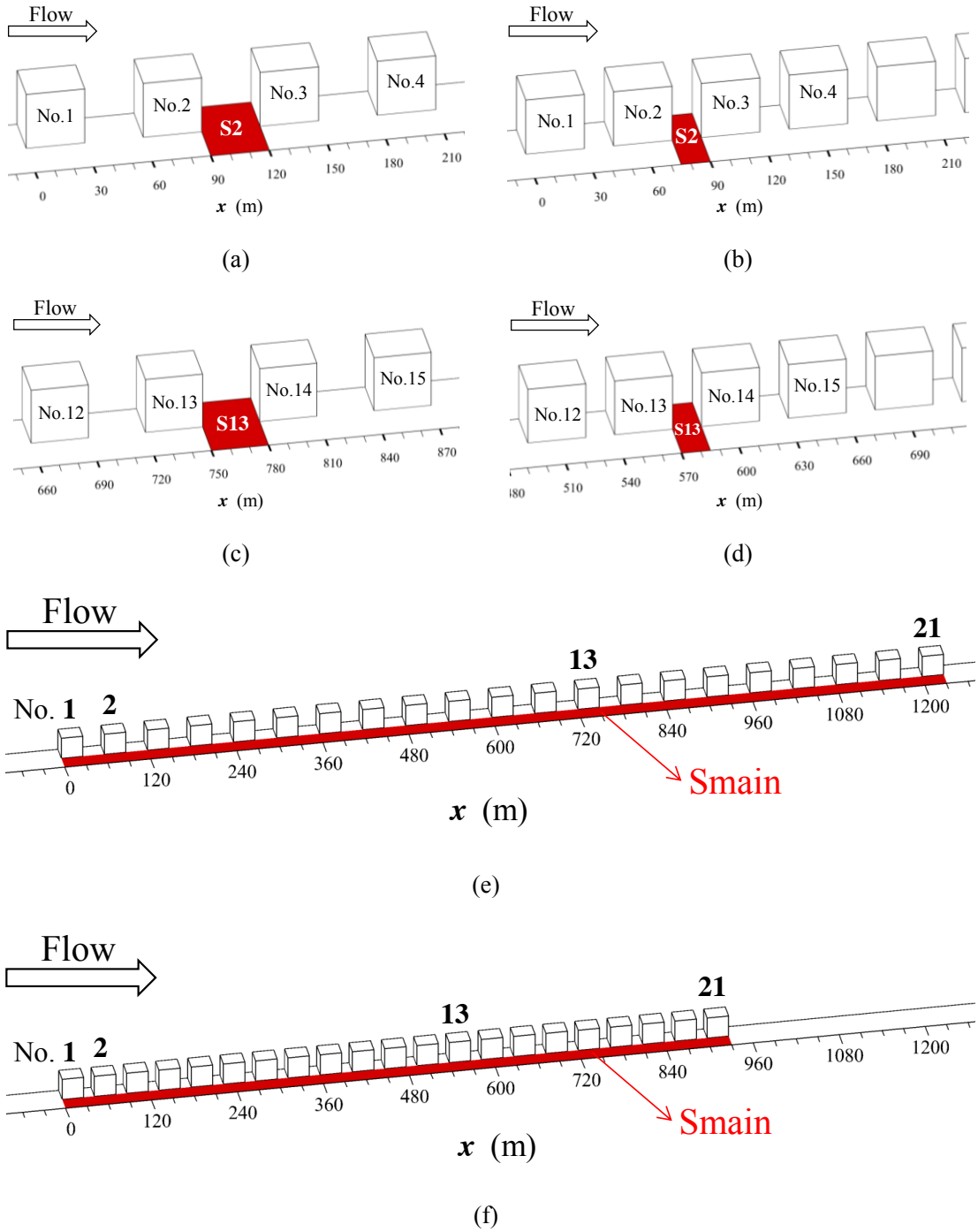

Fig.3 Descriptions of CO source settings: (a-b) S2, (c-d) S13 and (e-f) Smain in cases with H/Ws=1 and H/Ws=2.

CFD setups for advertisement boards and case descriptions

As depicted in Fig.4, nine kinds of advertisement boards arrangements were considered. Test cases are named as Case [*advertisement board type*, *street width of secondary streets (i.e. Ws*=15m or 30m*)*, *source location (i.e. S2, S13 or Smain)*]. Overall, total 39 test cases were investigated as summarized in Table 2. The type of "*None*" denotes the base case without any advertisement boards. As displayed in Fig.4a-4b, two kinds of basic arrangements of advertising boards were first investigated. "Leteral1 type" (Fig.4a, Case [Lateral1, *Ws*=30m/15m, S2 or S13]) represents "long" advertising boards (board length l_b=5m; board height h_b=2m) perpendicular to the building surface with 5m above the ground and uniformly 5m spaced. Meanwhile "Vertical1 type" (Fig.4b, Case [Vertical1, *Ws*=30m/15m, S2 or S13]) describes "tall" advertising board (board length l_b=2m; board height h_b=5m) attached to the buildings with 3m above the ground and 5m spaced. To avoid the difficulty in generating grid, all of the advertisement boards are ideally simplified as rectangles without thickness. Then as depicted in Fig.4c-4i, seven more complicated types of advertising board were introduced. In more detail, four kinds of lateral types (Fig. 4c-4f) are considered, including Leteral2_align type (Fig.4c) with the upper-layer advertising boards aligned to the original layer below, Leteral2_stagger type (Fig.4d) with upper-layer boards staggered to the original layer below, Lateral1_dense type (Fig.4e) with single-layer but denser advertisement boards (interval of 2.5m) than Lateral1 type (interval of 5m), Lateral1_lower type (Fig.4f)

with single-layer boards but only 3m high above the ground (2 m lower than Lateral1). Meanwhile, three kinds of vertical types were investigated (Fig.4g-4i), including Vercial2_align, Vertical2_stagger and Vertical1_dense, with similar settings as those for the corresponding Lateral types.

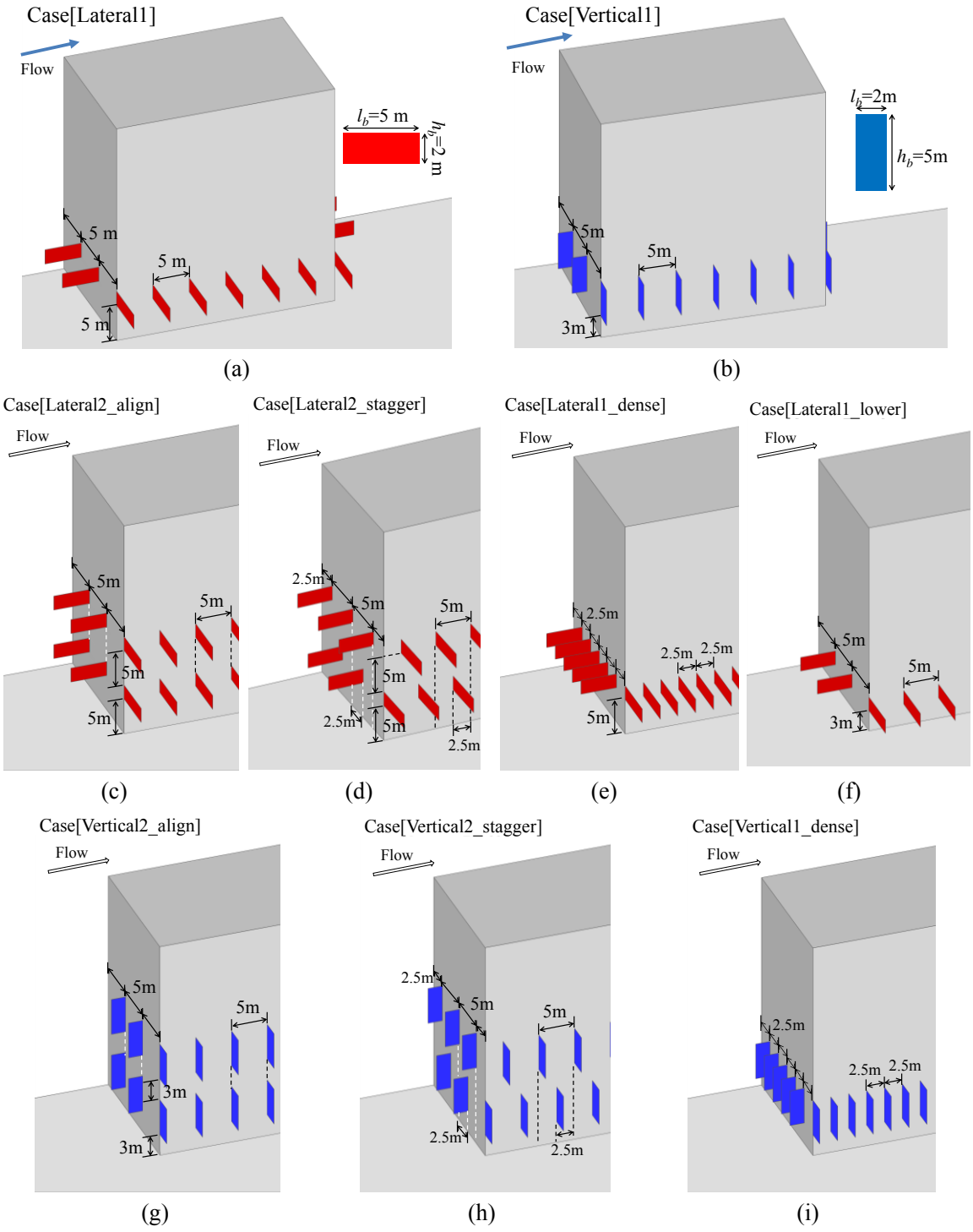

Fig.4 Detailed descriptions of advertisement boards' settings

354

355 **Table 2** Summary of test cases and advertising board models investigated

Case Name	Descriptions of advertising boards' arrangements
[None, *Ws**, Source**]	Without advertising boards
[Leteral1, *Ws*, Source]	Long advertising boards (length l_b=5m; height h_b=2m), 5m above ground, intervals of 5m (Fig.4a)
[Vertical1, *Ws*, Source]	Tall advertising boards (length l_b=2m; height h_b=5m) , 3m above ground, intervals of 5m (Fig.4b)
[Leteral2_align, *Ws*, Source]	An additional upper-layer of advertising board with same size and interval above, is align to the original layer. (Fig.4c)
[Leteral2_stagger, *Ws*, Source]	An additional upper-layer is staggered and locates above to the original layer below (Fig.4d)
[Leteral1_dense, *Ws*, Source]	Double advertising boards with half of the interval (5m to 2.5m) (Fig.4e)
[Leteral1_lower, *Ws*, Source]	Single-layer boards with only 3m high above ground (2 m lower than Lateral1) (Fig.4f)
[Vertical2_align, *Ws*, Source]	Same size as *Vertical1* and similar arrangement as Leteral2_align (Fig.4g)
[Vertical2_stagger, *Ws*, Source]	Same size as *Vertical1*and similar arrangement as Leteral2_stagger (Fig.4h)
[Vertical1_dense, *Ws*, Source]	Same size as *Vertical1* and same arrangement as . (Fig.4i)

356 ***Ws*** stands for the width of secondary streets (*Ws*=15m or 30m). As *Ws*=15m, only
357 *None*, *Letaral1* and *Vertical1* types are studied.
358 ****Source type*** includes **S2** (Fig.3a-3b), **S13**(Fig.3c-3d) and **Smain** (Fig.3e-f).

359

360 ## 4 CFD validation and grid independence study

361 ### 4.1 CFD validation of flow modelling

362 The reliability of CFD approaches using various *k-ε* models and standard wall

363 function was evaluated by wind tunnel data from Brown et al. [62]. In that wind
364 tunnel experiments (Fig.5a), an idealized urban model was built with 7 rows and 11
365 columns of cubic buildings with a parallel approaching wind to the main streets. Each
366 cubical building is 0.15m tall with the same space between buildings (i.e.
367 B=H=W=0.15m, H/W=1). The urban model was 1:200 scaled compared with the
368 full-scale models in case studies (as depicted in Section 3). As displayed in Fig.5a, x,
369 y and z are defined as the stream-wise, span-wise and vertical direction respectively.
370 x/H=0 denotes windward street entry and y/H=0 refers to the vertical center plane of
371 the middle building column. Vertical profiles of velocity components and turbulent
372 kinetic energy were measured at points of V_i (i=1-6) locating at y/H=0 and
373 x=1.5H-11.5H respectively (Fig.5a).

374 In the CFD validation case, a full-scale 7-row urban models (i.e. B=H=W=30m,
375 H/W=1) were considered with a scale ratio of 200:1 to wind-tunnel-scale models. Fig.
376 5b displays CFD domain and boundary conditions. As confirmed by experiments or
377 numerical simulations in the literature [32-33, 37, 53, 62-65], if the urban model is
378 sufficiently long in the span-wise direction, airflow in the middle column is hardly
379 influenced by the lateral urban boundaries. Thus, to reduce the computational time
380 and total grid number, the CFD validation case only considered half of the middle
381 column (Fig.5b), i.e. span-wise domain size Ly=30m.

382 Moreover, present urban model is 13H long. Urban boundaries are 9H, 6.7H and
383 40.3H from the domain roof, domain inlet and domain outlet. Zero normal gradient
384 boundary condition (i.e. outflow) was set for the domain outlet, and symmetry

boundary condition at the domain top and domain lateral boundaries. According to the literature [23, 33, 37-38, 62-65], vertical profiles of velocity $U_0(z)$, TKE $k(z)$ and its dissipate rate $\varepsilon(z)$ in Eq.(10-12) were defined at the domain inlet which are the same as those in cases studies described in Section 3.

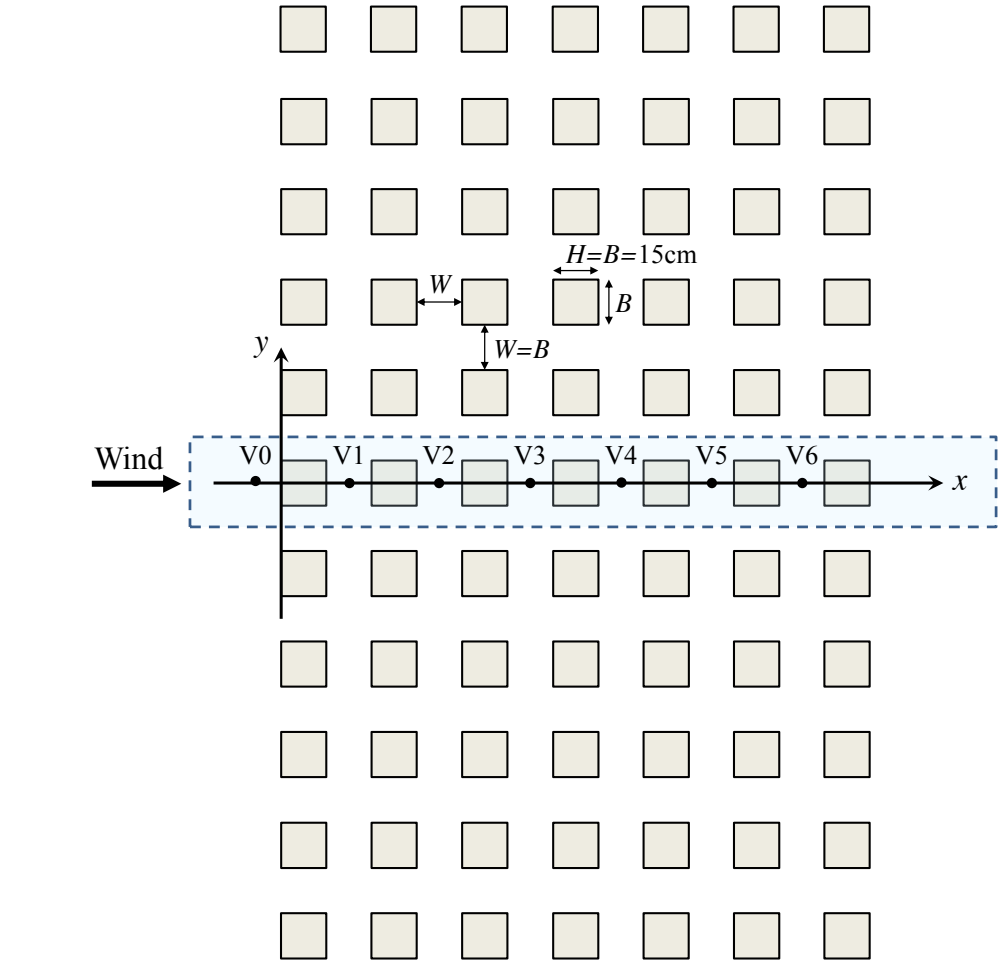

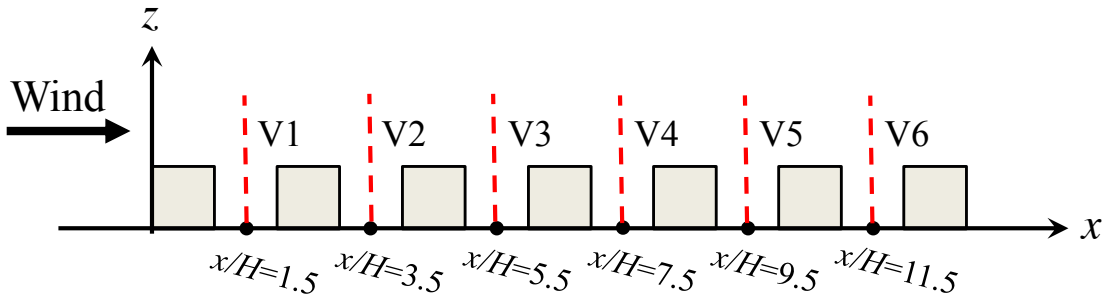

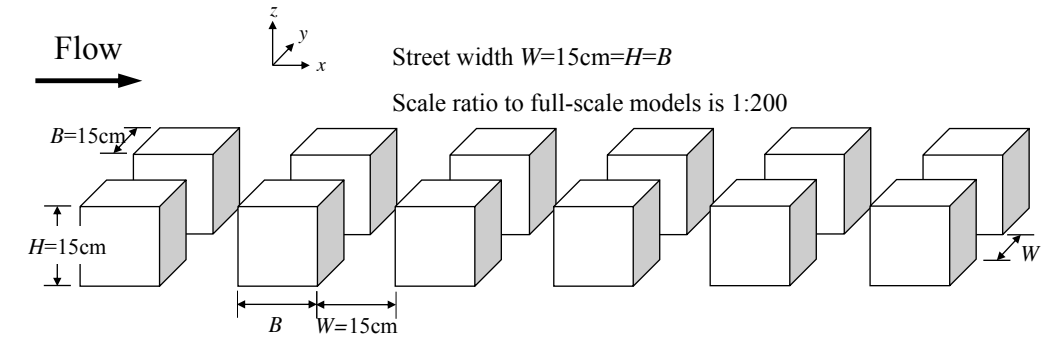

(a)

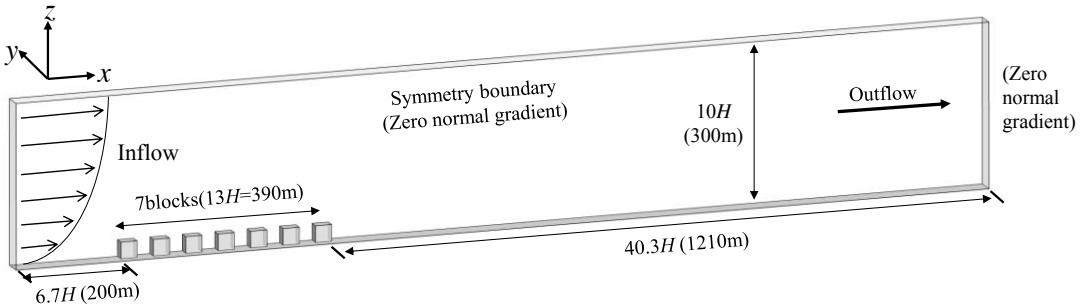

(b)

Fig.5 (a) Descriptions of wind tunnel experiment (Lien et al. [63]); (b) Computational domain in CFD validation case.

It is worth mentioning that, according to Snyder (1972) [69], if the reference Reynolds number $Re \gg 11000$, the turbulent flow pattern is Reynolds number independent, i.e. does not change with the increasing Reynolds number. The Reynolds number can be calculated as below:

$$Re = (U_{ref} \cdot H) / \nu \tag{13}$$

Here, U_{ref} is the reference velocity magnitude of the approaching free flow at building height ($z=H$) of wind tunnel models [62-63] (U_{ref}=3m/s).

In present studies, the reference Reynolds number in wind tunnel experiments is 3×10^4 with building height of H=15cm [62-63]. In full-scale simulation of the CFD

validation case, Re is 6×10^6 as H=30m with a scale ratio of 1:200. No matter wind-tunnel-scale models or full-scale models, both Re>>11000 and Reynolds number independence requirement is fully satisfied, thus in both scales the turbulent flow pattern is fully-developed and is not affected by the Re values.

Three grid arrangements were tested for grid independence study: fine grid (the minimum grid size next to wall surfaces was 0.1m, about 2.7 million hexahedral cells in total), medium grid (minimum grid size of 0.2m, about 1.5 million cells) and coarse grid (minimum grid size of 0.5m, about 0.6 million cells). All grid generation had the same grid expansion ratio of 1.15. Thus, there were at least four grids adopted in the pedestrian level (z=0-2m), which satisfy the grid requirement of the CFD guidelines [67-68]. As the normalized distance from wall surfaces y^+ ($y^+ = yu_\tau / \nu$) ranged from 30 to 500 at most regions of wall surfaces, standard wall function was set on all wall surfaces with no slip boundary condition [61].

Fig. 6 displays the vertical profiles of time-averaged stream-wise velocity $\overline{u}(z)$, vertical velocity $\overline{w}(z)$ and turbulence kinetic energy $k(z)$ in the CFD validation case with all three grid arrangements, comparing CFD results with wind tunnel data at some example points [62]. These figures infer that, as applying the standard k-ε model, CFD results with medium grids have little difference in contrast to that of the fine-grid case. In addition, with the medium grid arrangements, the standard k-ε model performs better than the RNG k-ε model, and the latter over-predicts both $\overline{u}$ and $\overline{w}$ as z<H but slightly underestimates the k profile. Therefore, by considering both numerical accuracy and reducing the computational time, the medium grid (i.e.

429 the minimum grid size of 0.2m next to wall surfaces) and the standard k-ε model are

430 adopted for further case studies.

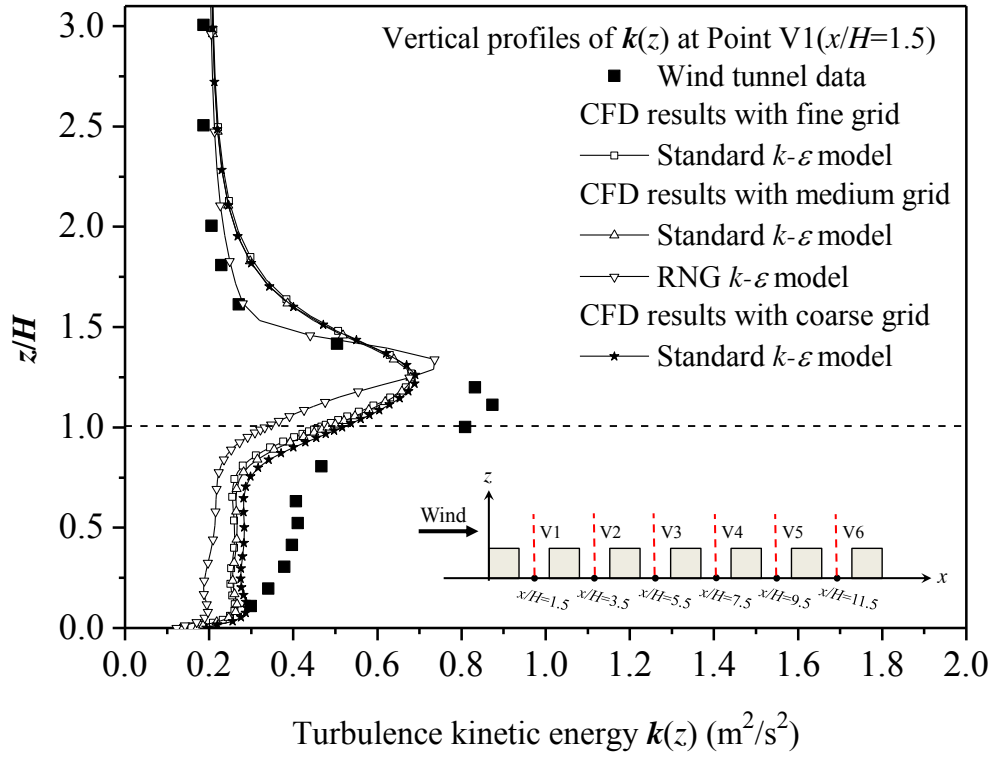

431

432 (a)

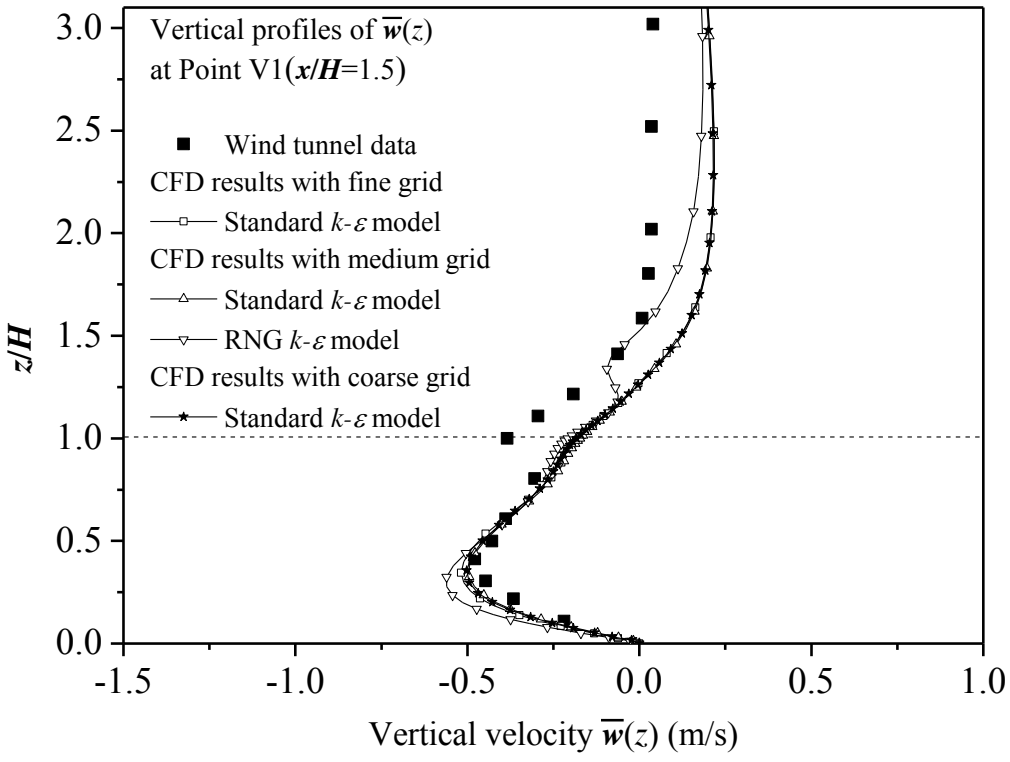

433

434 (b)

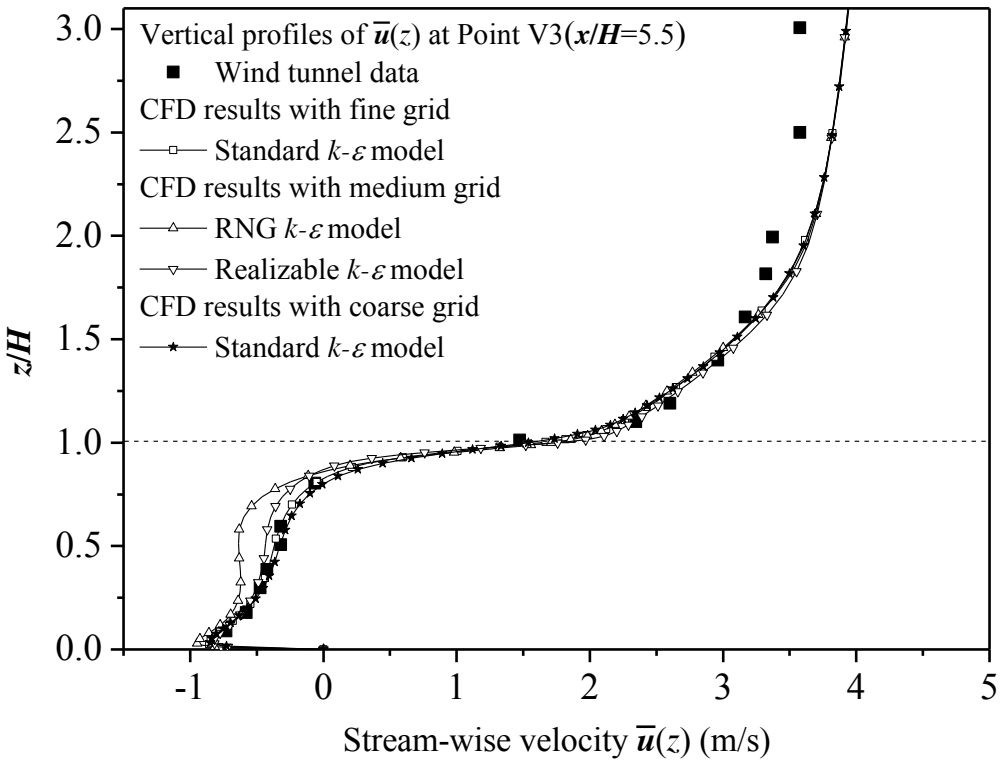

435

436 (c)

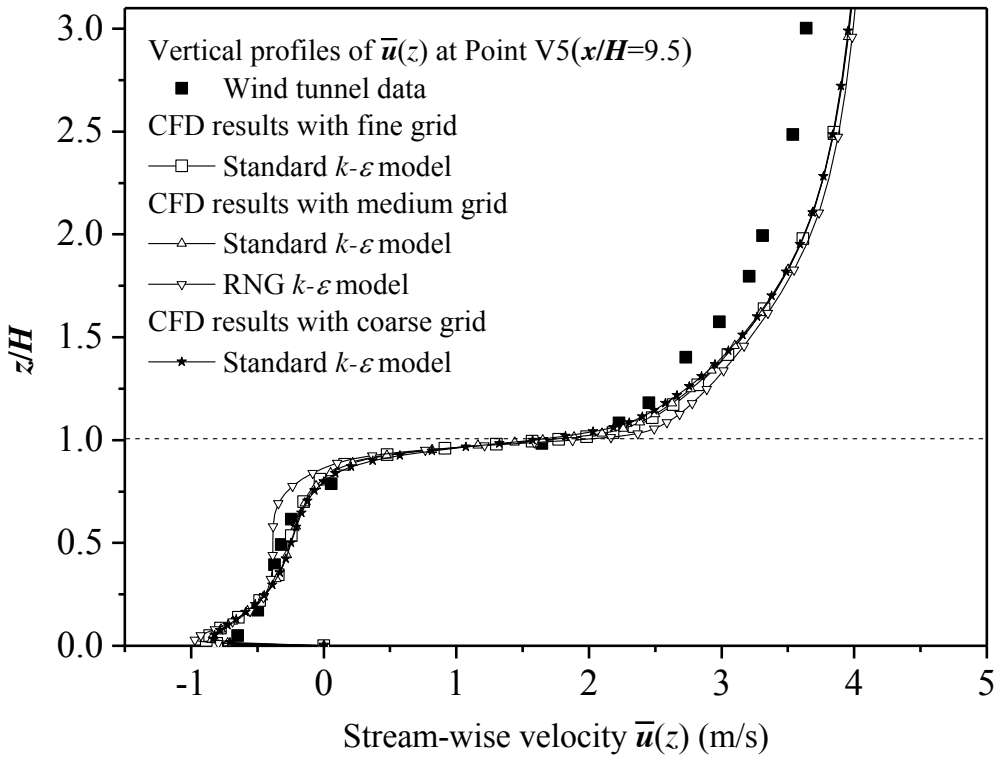

437

438 (d)

439 Fig.6 Vertical profiles in CFD validation case compared with wind tunnel data: (a)

440 $k(z)$ and (b) $\overline{w}(z)$ at Point V1, (c) $\overline{u}(z)$ at Point V3, (d) $\overline{u}(z)$ at Point V5.

441

To further quantify the numerical accuracy of the CFD method applied, several statistical performance metrics are calculated (Table 3), including mean value, the standard deviation (St dev.), the fraction of predictions (i.e. CFD results here) within a factor of two of observation (i.e. wind tunnel data here) (FAC2), the normalized mean error (NMSE), the fraction bias (FB) and the correlation coefficient (R). Here the NMSE refers to the normalized discrepancies between wind tunnel data and CFD results, and FB indicates overestimation or underestimation of predictions (i.e. negative value shows overestimation, and the positive value implies underestimation). According to the literature [70-71], a credible CFD simulation model should meet the following statistical metrics standards: FAC2$\geqslant$0.5, NMSE$\leqslant$1.5 and -0.3$\leqslant$FB$\leqslant$0.3. As shown in Table 3, $\overline{u}(z)$ at Points V3 and V5 as well as $k(z)$ at Point V1 fit the standards well. While $\overline{w}(z)$ at Point V1 performs a little poorly in the FAC2, but its correlation coefficient (R) is still acceptable as 0.9. In conclusion, present CFD methodologies using the standard k-ε model and the medium grid arrangement possess credible numerical accuracy in predicting urban airflow.

Table 3 Statistical performance metrics for CFD validation cases

Variable (position)		$\boldsymbol{k}$(z) (V1)	$\overline{\boldsymbol{w}}$(z) (V1)	$\overline{\boldsymbol{u}}$(z) (V3)	$\overline{\boldsymbol{u}}$(z) (V5)
Average					
	Wind tunnel	0.42	-0.21	1.47	1.58
	CFD	0.35	-0.12	1.54	1.69
Standard deviation					
	Wind tunnel	0.23	0.20	1.79	1.70
	CFD	0.15	0.27	1.87	1.85
FAC2		1.00	0.44	1.00	0.93
NMSE		0.15	0.65	0.01	0.02

FB	0.20	0.52	-0.05	-0.07
R	0.79	0.90	0.94	0.93

459

460 Finally, as Brown et al. [62] did not present the measurement result at the street
461 side (i.e. along the main street), as shown in Appendix (Fig. A1), the data of another
462 wind tunnel experiment was adopted to verify the effectiveness of the "half column
463 method" in the street side.

464

465 **4.2 CFD Validation of dispersion modelling**

466 The effectiveness of the standard k-ε model in predicting pollutant dispersion in
467 the idealized urban model is evaluated by wind tunnel experiment data by Chang and
468 Meroney [29]. Fig. 7a depicts the configuration of the wind-tunnel-scale urban model
469 adopted. Nine rectangular-prism building models (W=18.4cm, L=27.6cm, H=8cm)
470 were placed in a symmetric 3×3 arrangement with same separation distance
471 (B=2H=16cm). A point C_2H_6 (ethane) source located at the center point of the cross
472 street in front of the center building model. The concentration was measured at points
473 along the centerline of the windward wall of the center building model and the
474 leeward wall of the model ahead.

475 The same wind-tunnel-scale urban model was established in the CFD validation
476 case. Refer to Chang and Meroney [29], the evenly releasing C_2H_6 point source was
477 modeled as a 1.3×1.3cm velocity inlet with a constant vertically upward velocity as
478 0.05m/s and no turbulence. The mass fraction of C_2H_6 from that inlet was set to be 1.
479 Approaching flow velocity, turbulent kinetic energy (TKE) and its dissipation rate

(TED) profiles measured in that wind tunnel experiment were adopted at the simulation domain inlet [72]. No slip wall boundary condition was applied at both floor and all building facades. The total grid number was 816,102.

All the concentration results are presented in a dimensionless form K, which is defined as [29]:

$$K = CU_{ref}H^2 / Q \tag{14}$$

where C is the volume fraction of C_2H_6, U_{ref} denotes the free flow velocity at model height H, and Q is the flow rate of the steady source. Fig.7b shows that the prediction result of the standard k-ε model agrees well with the measured data, which captures both the scalar magnitude and the trend of K profiles. The result confirms that the standard k-ε model has a satisfactory prediction performance of pollutant dispersion.

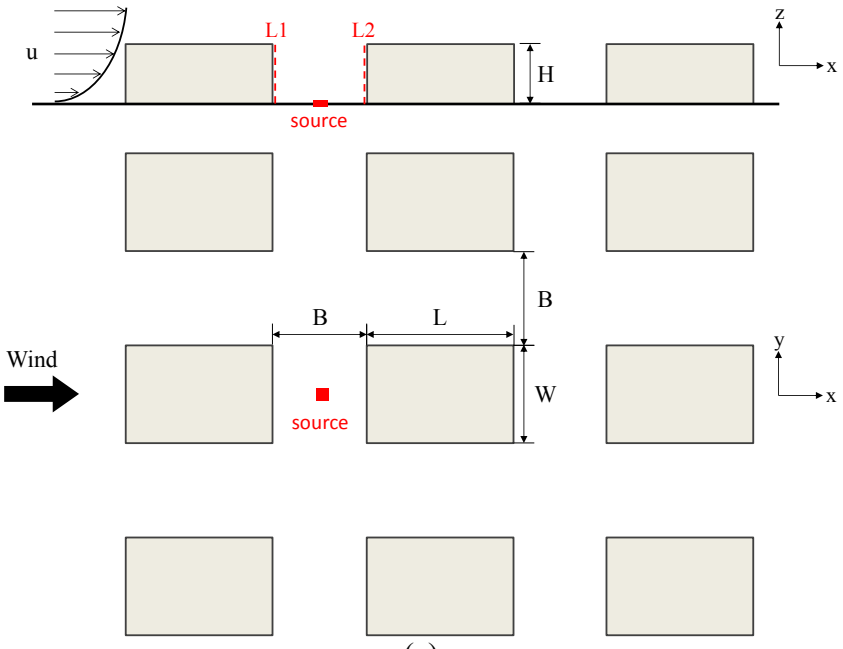

(a)

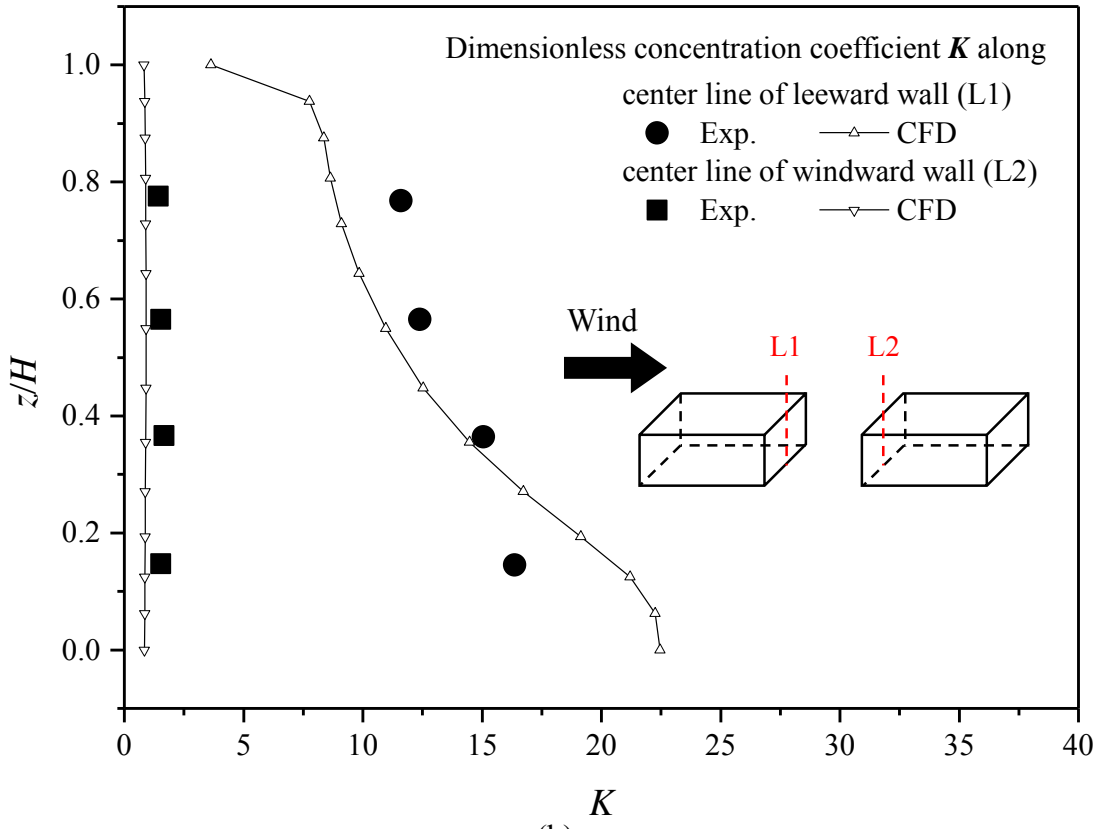

(b)

Fig.7 (a) Model configurations of wind tunnel experiment conducted by Chang and Meroney [29]. (b) Comparison of K between wind tunnel experiment result from Chang and Meroney [29] and CFD simulation applying standard k-ε model.

5 Results and discussion

5.1 Impacts of advertisement boards on flow and pollutant dispersion

Fig.8 displays velocity magnitude, 3D streamlines and CO concentration in the vertical plane of y=30m (the center plane of buildings, i.e. the domain symmetry boundary as shown in Fig.2d) in the target street (Street S2) for cases with 30m-wide secondary streets (H/Ws=1). 3D helical flow exits and the flow fields for cases with and without advertisement boards are similar in most regions (Fig.8a-8d). In addition, in contrast to case without advertisement boards, a little difference can be found that

the flow near building wall surfaces tends to go vertically along the vertical advertisement boards (Fig.8c-8d). Furthermore, advertisement boards slightly weaken the velocity near building surfaces (Fig.8a-8b), thus they slightly increase CO concentration near building walls (Fig.8e-8f). When CO source is fixed in Street 13 (Fig.3c, results not shown here), the overall velocity and concentration in Street 13 are slightly smaller and higher than those of Street S2. Similarly, advertisement boards in Street 13 also produce a decrease of velocity and an increase of CO concentration near building walls.

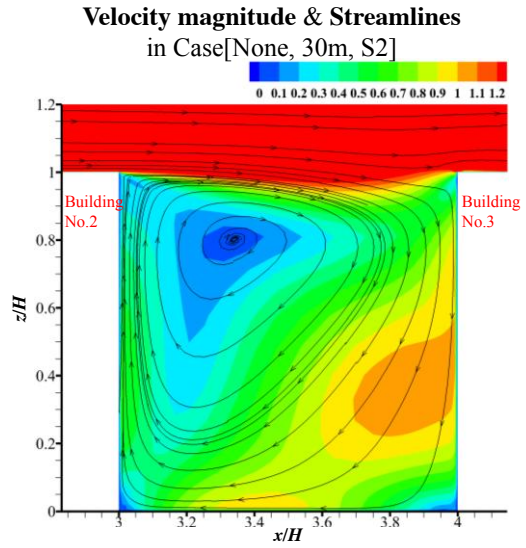

(a)

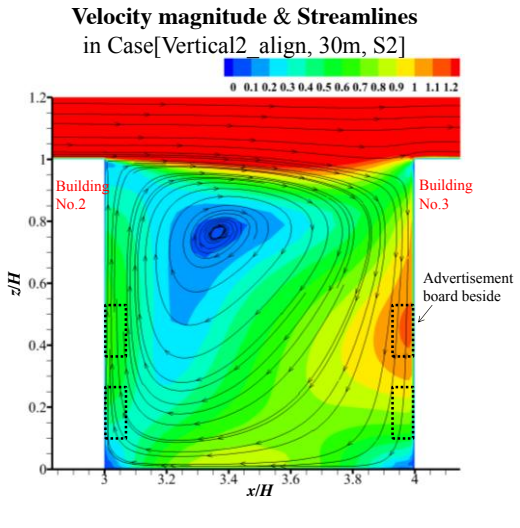

(b)

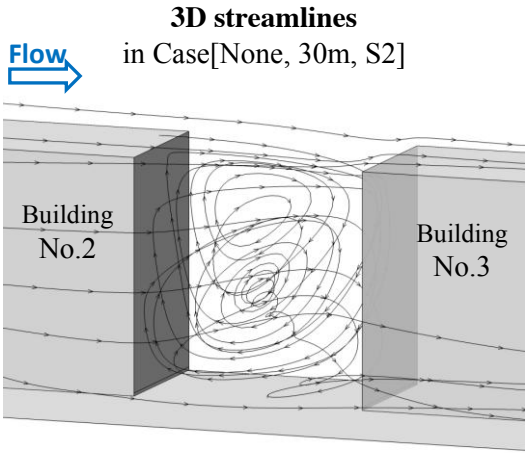

(c)

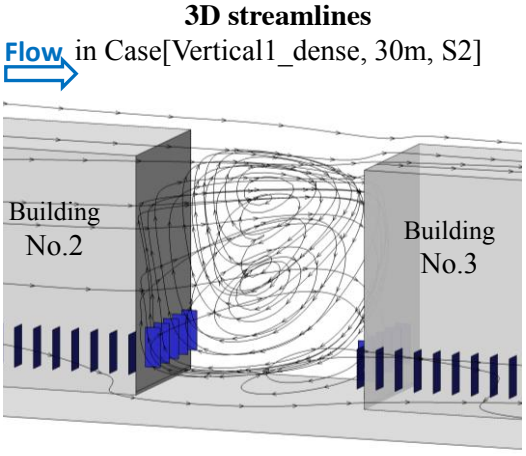

(d)

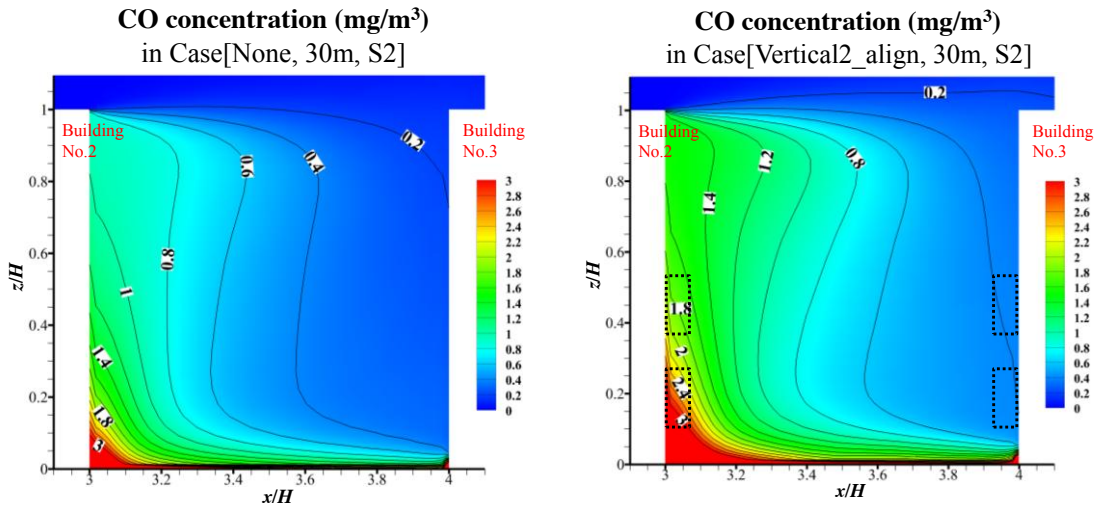

(e) (f)

Fig.8 (a-b) Velocity magnitude, (c-d) 3D streamlines and (e-f) CO concentration at y=30m in Street S2 in example cases with Ws=30m.

The concentration at building wall surfaces can be used to represent indoor concentration originated from outdoor pollutants when the buildings are naturally ventilated. Such concentration is more important to pollutant exposure analysis than that far from building walls. Thus Fig.9 further shows the concentration at building wall surfaces of Street 2 and Street 13 in example cases with H/Ws=1 (Ws=30m). For cases without advertisement boards, Fig.9a-9b confirm that leeward-wall concentration is always much higher than windward wall and both decrease toward the upper-level walls.

In contrast to Fig.9a-9b, the advertisement boards in Fig.9c-9f are found to significantly or slightly raise the leeward-side concentration, and more pollutants are dispersed upwardly. Moreover, Fig. 9c-9d verifies that double-layer advertisement boards (e.g. Lateral2_align) produce higher concentration and induce more upward

CO dispersion than single-layer type (e.g. Lateral1). Fig. 9e shows CO concentration distribution with dense advertisement boards (e.g. Vertical1_dense) is similar with that of type Vertical1. Finally, Fig.9f confirms that the two-layer type with staggered arrangements (e.g. Vertical2_stagger) even slightly decrease CO concentration than the aligned type (e.g. Vertical2_align).

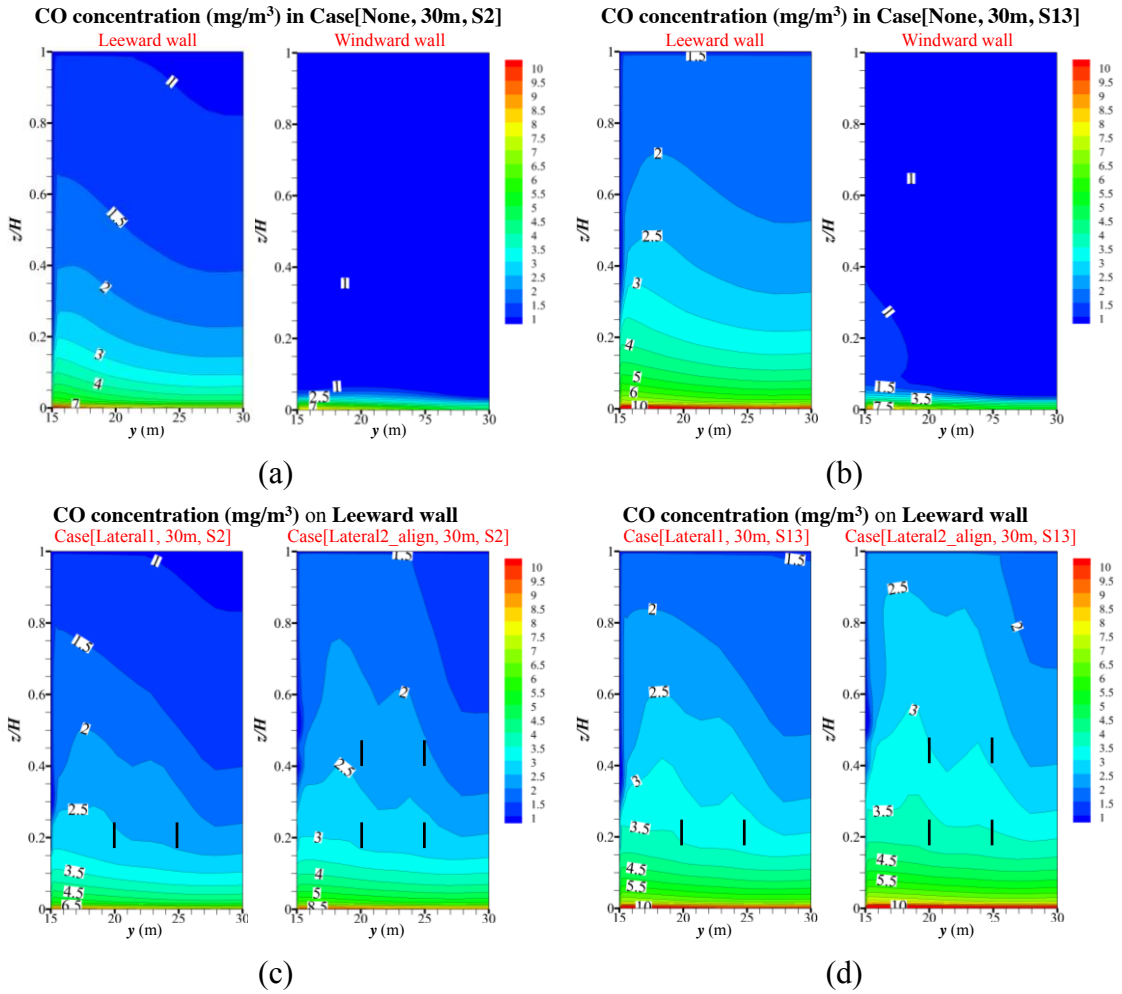

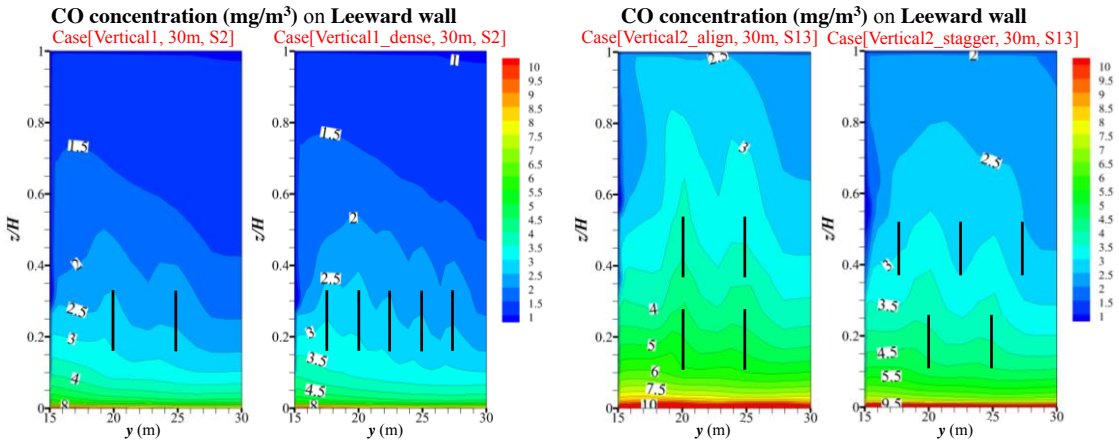

(e) (f)

535 Fig.9 CO concentration on building walls next to target street (*Ws*=30m) in (a)
536 Case[None,30m,S2] and (b) Case[None,30m,S13]; CO concentration on leeward wall
537 of target street in example cases with (c-d) lateral-type and (e-f) vertical-type
538 advertisement boards. (Black lines in (c-f) stands for the location of advertisement
539 boards on the building walls.)

540

541 Fig. 10 compares the flow and concentration filed in Street 2 (*Ws*=30m or 15m)
542 with local CO source. Different 3D downward helical flows are produced
543 (Fig.10a-10b). Velocity in narrower street (Fig.10d) is slightly smaller than that in
544 wider street (Fig. 10c), especially near the ground. As a result, dispersion
545 characteristics are different. Wider Street 2 experiences higher leeward-side
546 concentration than the windward-side (Fig.10e), however it is opposite in narrower
547 Street 2 (Fig.10f). This difference can be explained by the CO concentration at *z*=1m
548 (Fig.10g), the downward helical flows attack the ground and subsequently induce the
549 lateral flows from the secondary streets to the main streets, however the direction of
550 such ground-level lateral flows are different, i.e. toward leeward wall in case with

551 wider secondary street but flowing to windward wall in the narrower one.

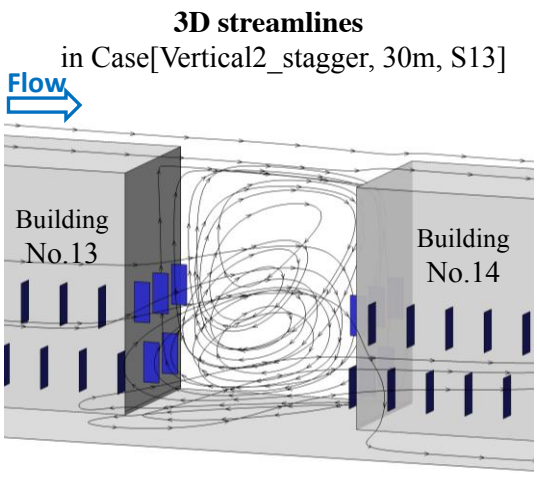

(a)

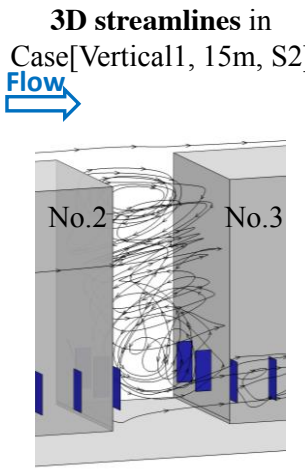

(b)

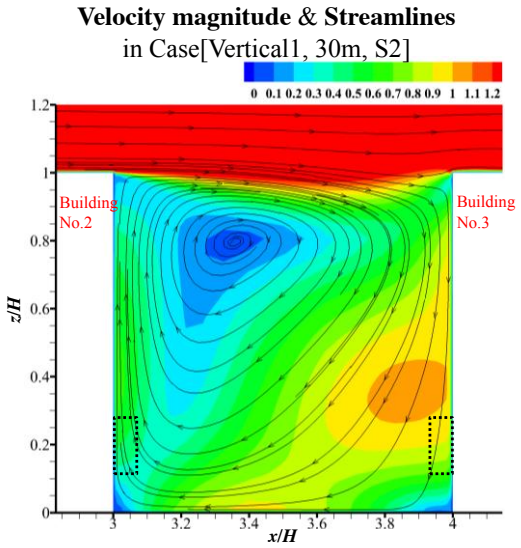

(c)

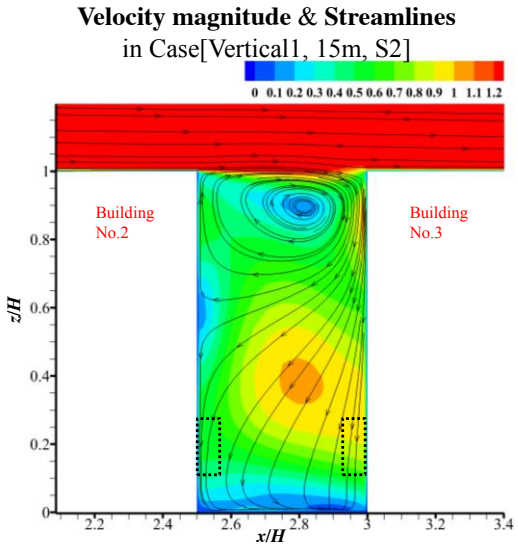

(d)

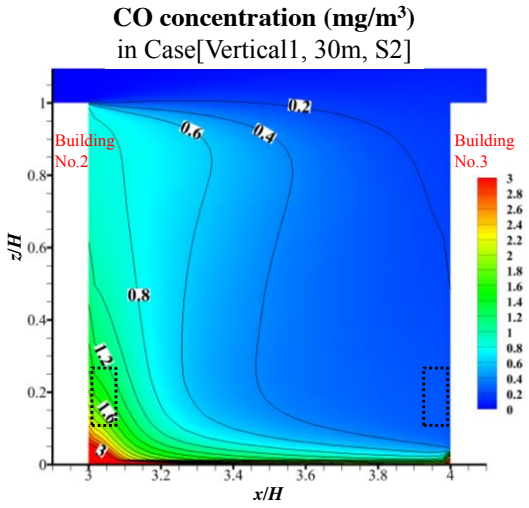

(e)

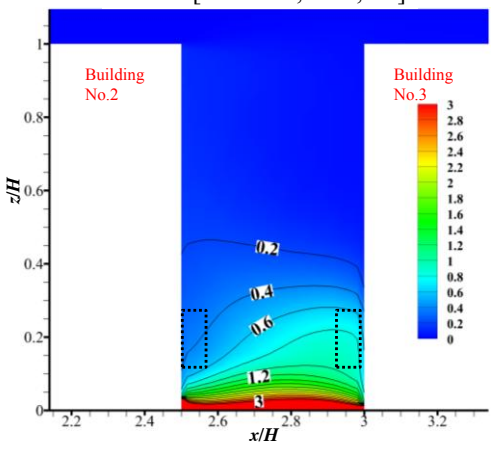

(f)

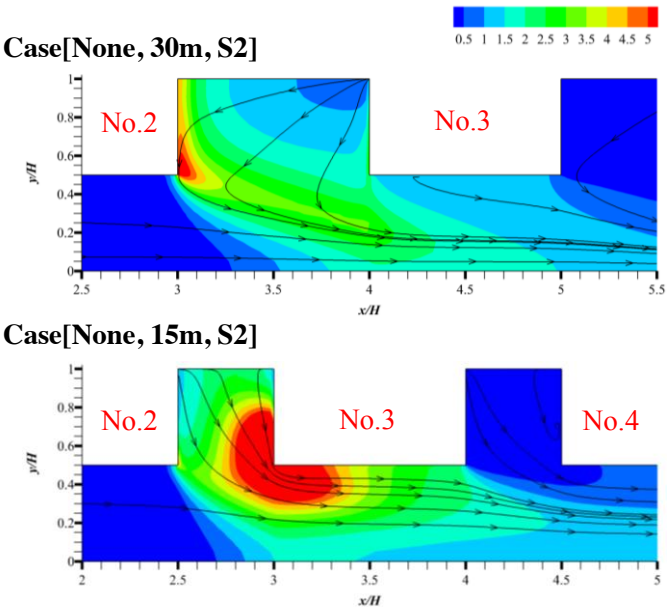

(g)

552 Fig.10 (a-b) 3D streamlines , (c-d) Velocity magnitude, (e-f) CO concentration filed
553 at *y*=30m in Street 2 in example cases with *Ws*=15m; (g) CO concentration and
554 streamlines in plane of *z*=1m in Case[None,15m,S2] and Case[None,30m,S2].

555

556 Then Fig.11a-11d further display the flow and concentration at windward and
557 leeward building walls in cases with narrower Street 2 and 13 (*Ws*=15m) without
558 advertisement boards. Results show that, the concentration on windward building
559 walls is much higher than leeward walls and less pollutant is dispersed upwardly in
560 15m-wide cases (Fig.11a-11b) than 30m-wide cases (Fig. 9a-9b). Furthermore, it is
561 surprise to find cases with narrower Street 2 (Fig.11a) experience much higher
562 windward-wall concentrations than Street 13 cases (Fig.11b), which is opposite to
563 cases with wider secondary streets (*Ws*=30m, Fig.9). Such dispersion characteristics
564 can be explained by Fig.11c-11d that the downward helical flow in Street 13 has a

565 larger downward velocity near the windward wall than Street 2, which produces more
566 ground-level lateral pollutant transportation to the main street (Fig.11g) and less
567 upward pollutant dispersion (Fig.11a-11b). Then Fig.11e-11f emphasize the
568 windward-wall concentration (i.e. highly polluted region) in Street 2 and Street 13
569 with advertisement boards. In contrast to Fig.11a-11b, the advertisement boards
570 slightly enhance the upward pollutant dispersion and raise windward-wall
571 concentration more or less. Besides, vertical-type advertisement boards produce more
572 upward pollutant transport than lateral-type (Fig.11e-11f).

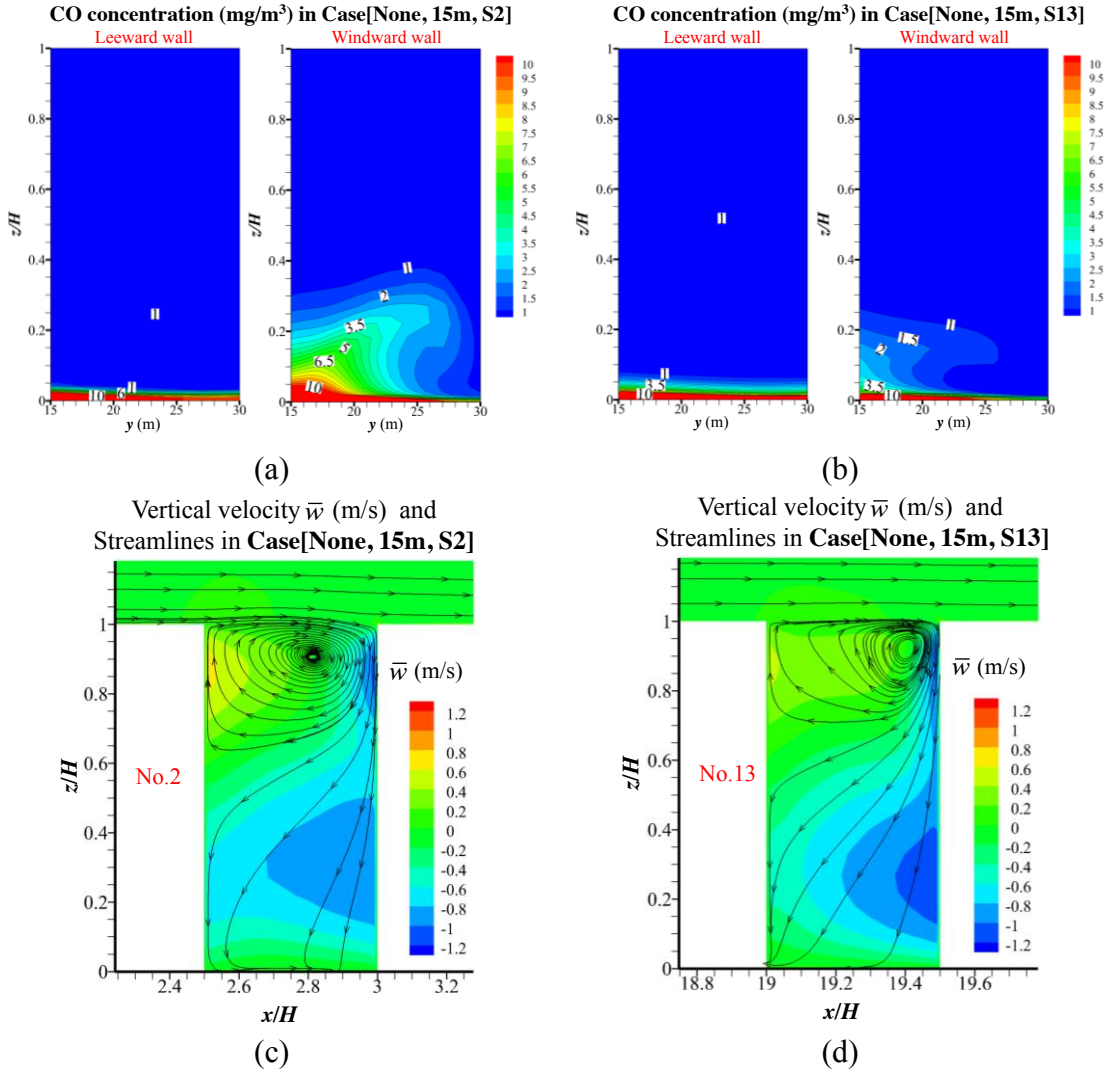

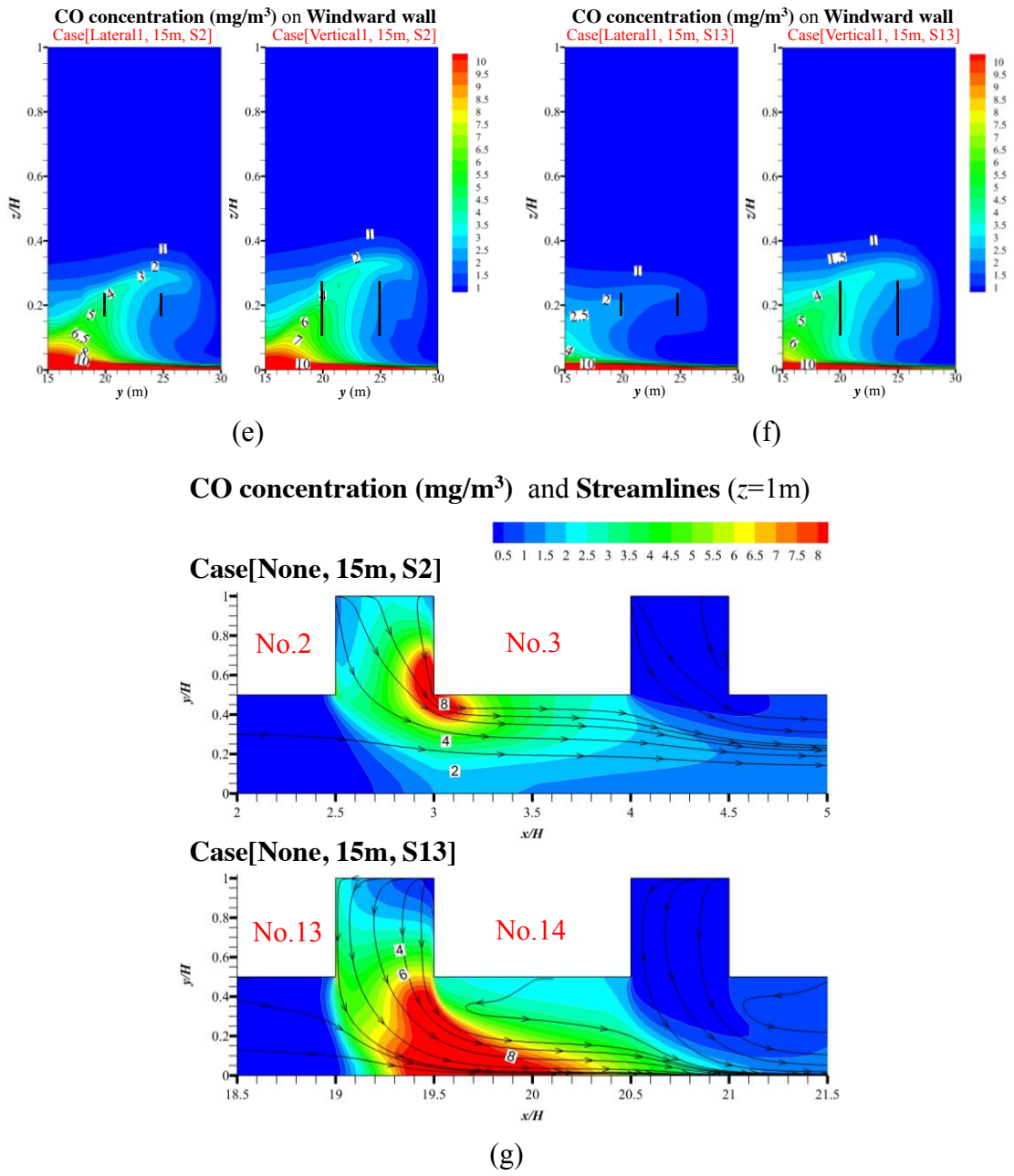

573 Fig.11 CO concentration on building walls next to 15m-wide target street (a) S2 and
574 (b) S13; (c-d) velocity magnitude at *y*=30m and (e-f) windward-wall CO
575 concentration in example cases as *Ws*=15m; (g) CO concentration and streamlines in
576 *z*=1m in Case[None,15m,S2] and Case[None,15m,S13]. (Black lines in (e-f) stands
577 for the location of advertisement boards on the building walls.)

578

579 **5.2 Impacts of advertisement boards on building intake fraction with S2 and S13**

5.2.1 *P_iF* on leeward and windward walls of target streets

This subsection mainly analyzes the impacts of advertisement board settings on personal intake fraction (*P_iF*) at various heights on building walls of Street 2 and 13.

Fig.12a-12b shows vertical profiles of *P_iF* along windward and leeward walls in some example cases with wider Street 2 (*Ws*=30m) and lateral-type or vertical-type advertisement boards. First, no matter with or without advertisement boards, leeward-side *P_iF* is always much larger than windward-side and *P_iF* decreases quickly from pedestrian levels towards upper levels (Fig.12a-12b). Moreover, Fig.12a shows that, in contrast to cases without advertisement board, the single-layer lateral type (i.e. Lateral1) slightly raise *P_iF*, and the double-layer Lateral2 type can increase *P_iF* more considerably, especially at upper levels. In addition, the impacts of vertical-type advertisement boards (Fig.12b) on *P_iF* profiles are similar with lateral-type cases. In particular, vertical-type cases experience greater overall *P_iF* than lateral-type cases, especially for Vertical2_align type with double-layer aligned boards. These findings are consistent with the concentration distribution in Fig. 9.

Fig. 12c compares vertical profiles of *P_iF* in 15m-wide or 30m-wide cases with source S2. As discussed in subsection 5.1, for all 15m-wide cases, the particular downward helical flows significantly weaken the upward pollutant dispersion and tend to transport more CO toward low levels of windward wall. As a result, 15m-wide cases experience greater windward-side *P_iF* than leeward-side, opposite to 30m-wide cases. In particular, the ground-level maximum *P_iF* are 5.89 and 7.15 ppm for Case [None, 15m, S2] and Case [Lateral1, 15m, S2] respectively (not shown

602 in Fig. 12c) at windward walls, nearly 3 times as the maximum *P_iF* in Case [None,
603 30m, S2] (2.62 ppm at leeward wall). Moreover, narrower secondary streets
604 (15m-wide) experience much less *P_iF* in its upper level (z/H>0.5) than 30m-wide
605 cases, especially for their windward walls. For example, *P_iF* in the upper-level
606 windward and leeward walls of Case [None, 30m, S2] are 0.084-0.054ppm and
607 0.411-0.223ppm respectively (from z/H=0.62-1), while those for Case [None, 15m, S2]
608 are 0.025-0.004ppm and 0.041-0.014 ppm from z/H=0.62-1.

609 Then Fig. 12d-12f emphasizes vertical profiles of *P_iF* as CO source moves to
610 the downstream Street 13 (i.e. S13). First, Fig. 12d displays *P_iF* profiles in
611 30m-wide S13 cases with vertical-type advertisement boards. Similarly, all kinds of
612 vertical types produce larger leeward-side *P_iF* than that without advertisement
613 boards (”none” type), and leeward-side *P_iF* with S13 (Fig. 12d) significantly exceed
614 those with S2 (Fig. 12b). Furthermore, Fig. 12e compares *P_iF* in S13 cases with
615 15m-wide and 30m-wide secondary streets. Likewise, 15m-wide cases experience
616 larger windward-side *P_iF* than the leeward-side, opposite to that of 30m-wide cases.
617 Besides, compared with the 15m-wide case without advertisement boards, Vertical1
618 type significantly raises windward-side *P_iF* than Lateral1 type. Finally Fig. 12f
619 makes a comprehensive comparison (15m-wide to 30m-wide, S13 to S2) between all
620 cases without advertisement boards. It is clear that, for 30m-wide cases, the
621 downstream street (S13) experiences weaker airflow and subsequently attains slightly
622 greater *P_iF* than S2. However, as confirmed by Fig. 11a-11b in Subsection 5.1, those
623 for 15m-wide cases are opposite, i.e. S13 cases attain smaller *P_iF* than S2 cases.

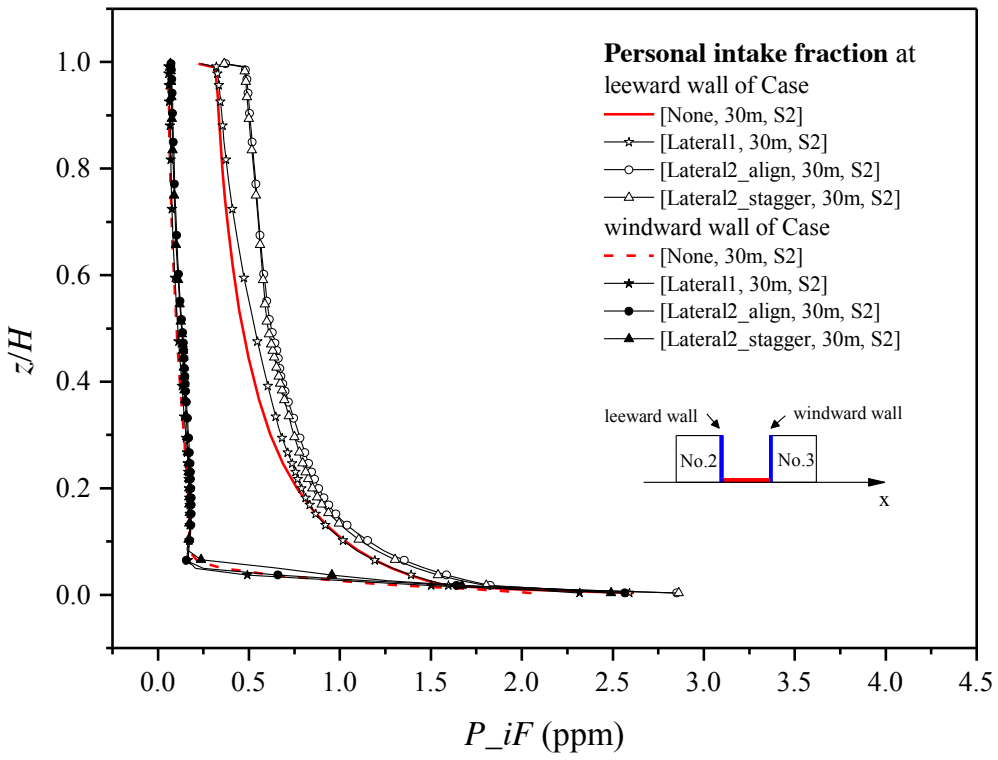
Personal intake fraction at
leeward wall of Case
[None, 30m, S2]
[Lateral1, 30m, S2]
[Lateral2_align, 30m, S2]
[Lateral2_stagger, 30m, S2]
windward wall of Case
[None, 30m, S2]
[Lateral1, 30m, S2]
[Lateral2_align, 30m, S2]
[Lateral2_stagger, 30m, S2]
leeward wall
windward wall
No.2
No.3
x
z/H
P_iF (ppm)

(a)

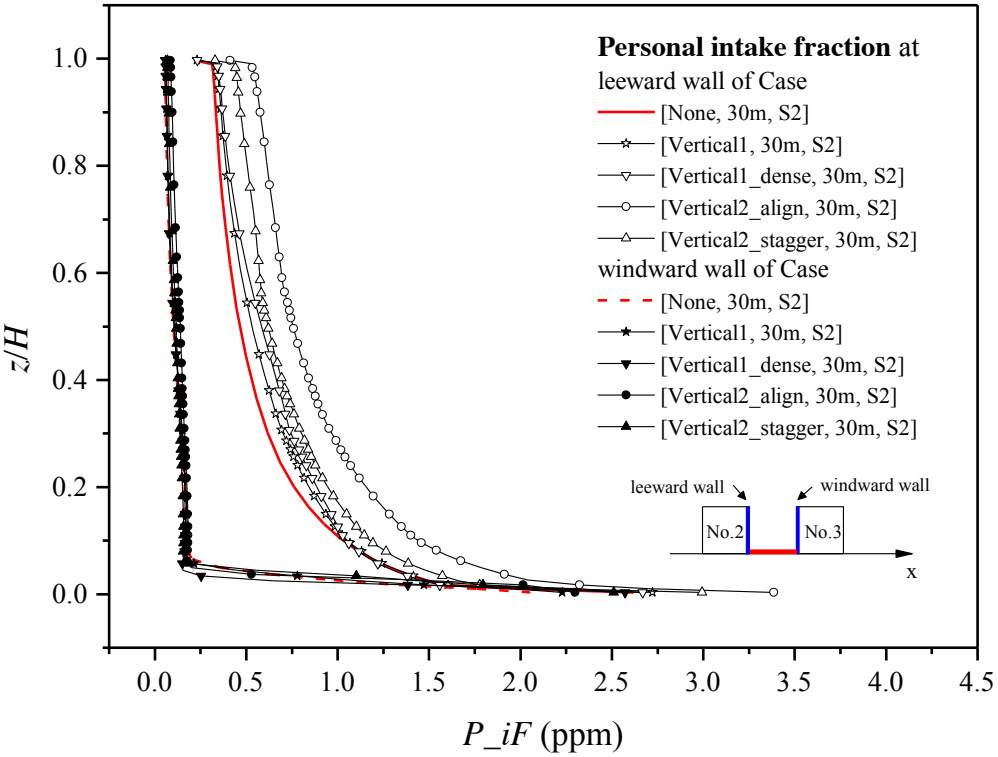
Personal intake fraction at
leeward wall of Case
[None, 30m, S2]
[Vertical1, 30m, S2]
[Vertical1_dense, 30m, S2]
[Vertical2_align, 30m, S2]
[Vertical2_stagger, 30m, S2]
windward wall of Case
[None, 30m, S2]
[Vertical1, 30m, S2]
[Vertical1_dense, 30m, S2]
[Vertical2_align, 30m, S2]
[Vertical2_stagger, 30m, S2]
leeward wall
windward wall
No.2
No.3
x
z/H
P_iF (ppm)

(b)

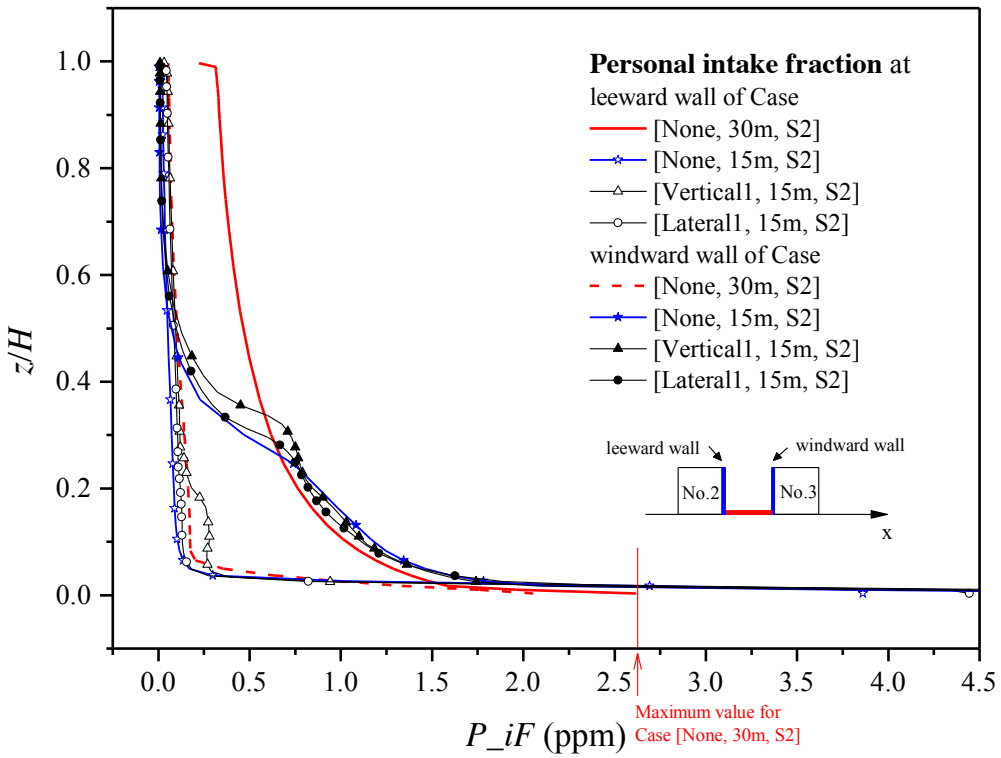

628

629 (c)

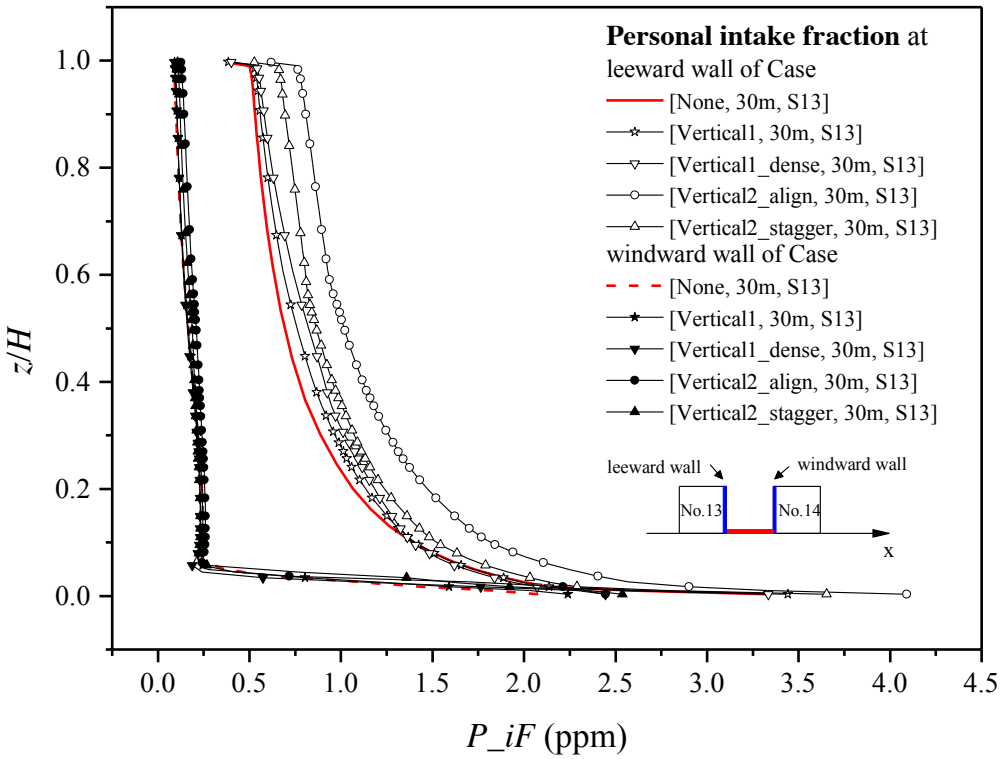

630

631 (d)

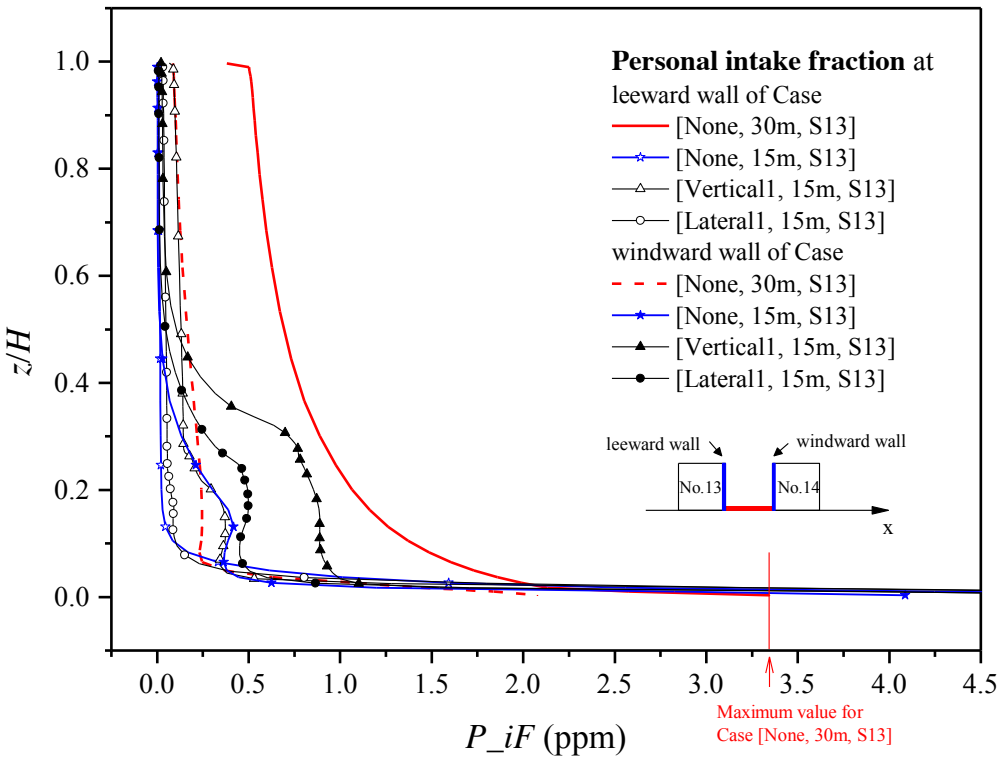

(e)

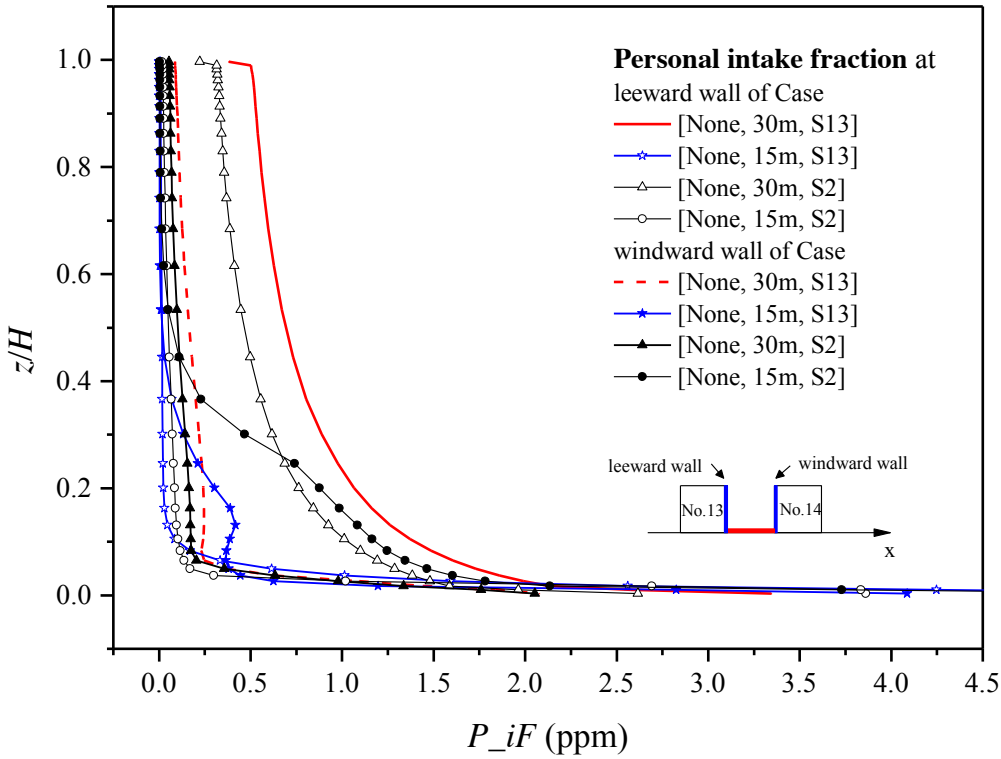

(f)

Fig.12 Vertical profiles of *P_iF* along building walls in example cases next to (a-c) target street 2, (d-e) next to target street 13, and (f) comparisons between cases with

638 CO source S2 and S13 without advertisement boards.

639

640 Finally, Fig. 13a displays the overall surface-averaged *P_iF* ($<P\_iF>_T$) for both
641 leeward and windward wall of the target street for all cases. Obviously, 15m-wide
642 cases with *H*/*Ws*=2 attain smaller $<P\_iF>_T$ (0.155-0.339ppm) than 30m-wide cases
643 (*H*/*Ws*=1, 0.375-0.731ppm). Such finding is opposite to that of 2D street canyons in
644 He et al. [10], in which $<P\_iF>_T$ in 2D deeper streets (5.64ppm as *H*/*Ws*=2) is larger
645 than that in 2D shallower streets (4.42ppm as *H*/*Ws*=1). Furthermore, $<P\_iF>_T$ in
646 present 3D cases (0.155-0.731ppm) are one-order smaller than those of 2D cases
647 (4.42-5.64ppm). Such phenomena can be explained as below: 3D urban models are
648 ventilated by both the flow flushing 3D urban space and turbulent diffusion/air
649 exchange across street roofs, thus experience much stronger pollutant dispersion
650 capacity than 2D street canyons in which wind is relatively weak and pollutants can
651 only be removed across street roof. All advertisement boards basically raise $<P\_iF>_T$
652 more or less (Fig. 13a), and cases with double-layer advertisement boards experience
653 larger $<P\_iF>_T$ than single-layer types, especially Case [Vertical2_align, 30m]
654 experience the greatest $<P\_iF>_T$ among all the cases (i.e. $<P\_iF>_T$ for S2 and S13 are
655 47.5%-36.9% greater than Case [none, 30m]). In more detail, Fig. 13b shows <*P_iF*>
656 at leeward wall and windward wall respectively. Table 4 displays the ratios of
657 leeward-side <*P_iF*> to windward-side <*P_iF*> ($<P\_iF>_{lee/wind}$). For 30m-wide cases,
658 leeward-side <*P_iF*> are 3.71-4.70 times of windward-side <*P_iF*> with S2 source
659 and 3.73-4.53 times with S13 source, while for 15m-wide cases $<P\_iF>_{lee/wind}$ are all

660 below 1 (i.e. 0.339- 0.931) verifying leeward-side <*P_iF*> are smaller than

661 windward-side.

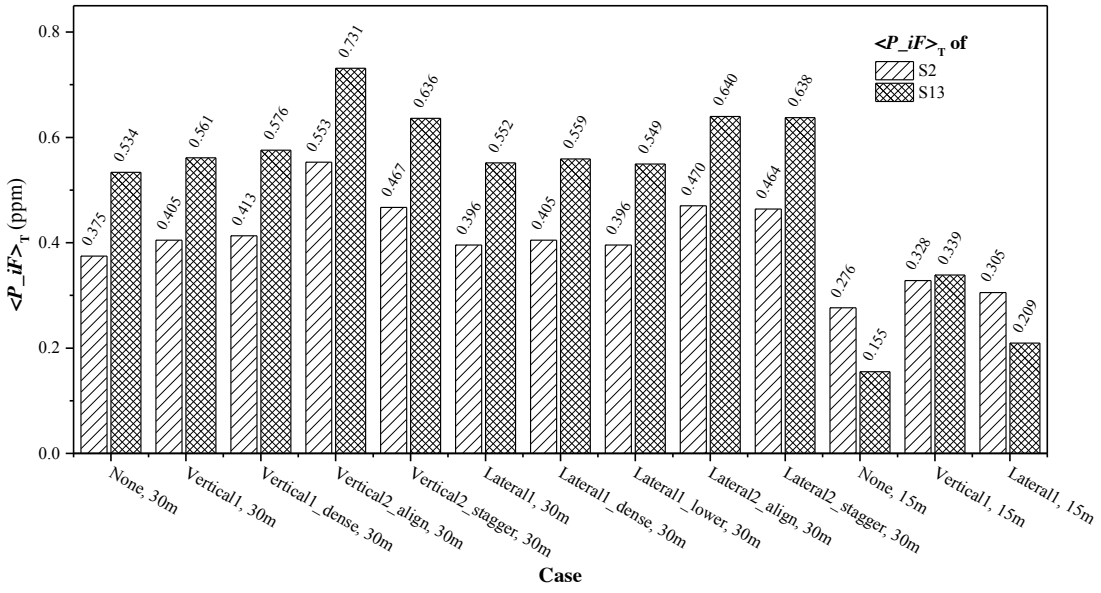

662

663 (a)

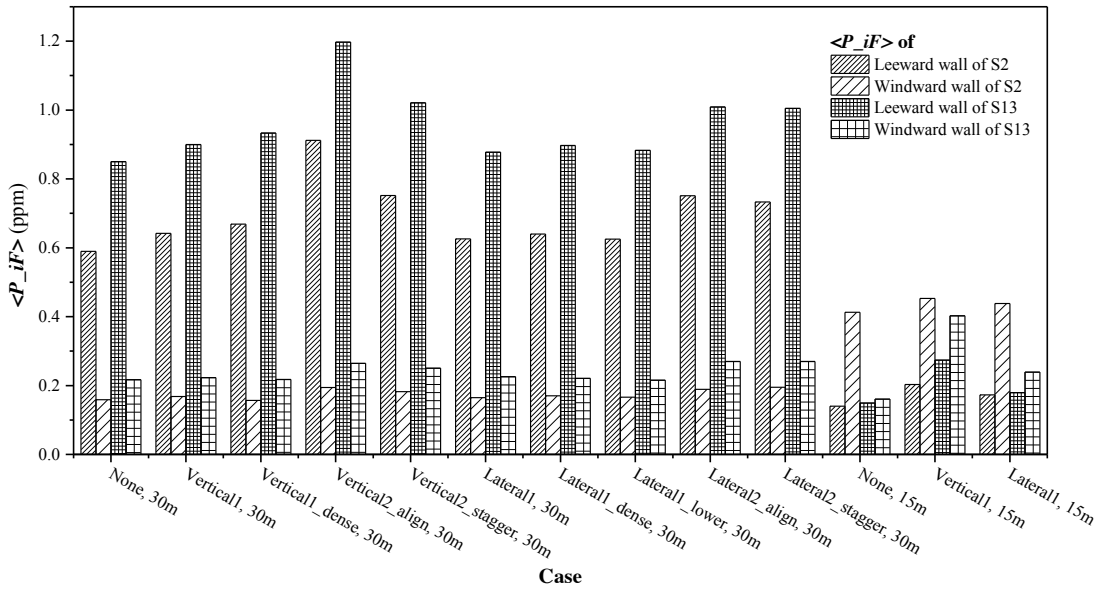

664

665 (b)

666 Fig.13 (a) Overall surface-averaged <*P_iF*> value of entire target street (<*P_iF*>$_T$)

667 and (b) surface-averaged *P_iF* (<*P_iF*>) of leeward and windward walls respectively.

668

669 **Table 4** <*P_iF*>$_{lee/wind}$ for all cases studied

Case name	**Source S2**	**Source S13**

Case[None, 30m]	3.710	3.923
Case[Vertical1, 30m]	3.821	4.037
Case[Vertical1_dense, 30m]	4.261	4.293
Case[Vertical2_align, 30m]	4.701	4.524
Case[Vertical2_stagger, 30m]	4.132	4.072
Case[Lateral1, 30m,]	3.794	3.892
Case[Lateral1_dense, 30m]	3.765	4.059
Case[Lateral1_lower, 30m]	3.765	4.101
Case[Lateral2_align, 30m]	3.974	3.739
Case[Lateral2_stagger, 30m]	3.759	3.726
Case[None, 15m]	0.339	0.931
Case[Vertical1, 15m]	0.448	0.681
Case[Lateral1, 15m]	0.395	0.749

*$\langle P\_iF \rangle_{lee/wind}$: ratios of leeward $\langle P\_iF \rangle$ to windward $\langle P\_iF \rangle$.

5.2.2 $\langle P\_iF \rangle_B$ profiles toward downstream streets

Building intake fraction $\langle P\_iF \rangle_B$ represents the spatially-averaged P_iF at all wall surfaces of each building model. This subsection emphasizes the influence of advertisement boards and CO source locations on the decreasing processes of $\langle P\_iF \rangle_B$ from the target street to downstream urban regions (Fig. 14). Only cases with 30m-wide secondary streets are discussed here.

Fig. 14a depicts $\langle P\_iF \rangle_B$ for three example cases (None, Lateral1 and Vertical1) with CO source S2 or S13. Obviously, $\langle P\_iF \rangle_B$ decreases exponentially from the building adjoining the target street toward downstream regions. With CO source S13, since wind in Street 13 is relatively weaker than Street 2, thus more CO accumulates in Street 13 and $\langle P\_iF \rangle_B$ are much greater nearby S13 than Street 2. Moreover, $\langle P\_iF \rangle_B$ in S13 cases decrease more quickly toward downstream streets. Then Fig. 14b-14c display $\langle P\_iF \rangle_B$ profiles in more 30m-wide test cases. All types of advertisement boards raise $\langle P\_iF \rangle_B$ more or less than cases without advertisement

686 boards. In addition, no matter for lateral-type (Fig. 14b) or vertical-type (Fig. 14c)
687 advertisement boards, double-layer types (Vertical2 or Lateral2, aligned or staggered)
688 attain much greater $<P\_iF>_B$ near the target street with CO source. However, for
689 buildings in far downstream regions, those double-layer-type cases experience a little
690 smaller $<P\_iF>_B$ as more CO is accumulated in the target street.

691 To quantify the influence of advertisement boards on $<P\_iF>_B$ decreasing rates
692 towards downstream, the decay function as $<P\_iF_n>_B = a \times <P\_iF_{n_0}>_B \times e^{(n_0-n)/b}$
693 (n=building number; for S2 or S13 cases, n_0=3 or 14) is defined. Table 5 summarizes
694 the exponentially decay factor ***b*** for all 30m-wide case. Larger decay factor b
695 indicates relatively mild decreasing of $<P\_iF>_B$ profile. The decay factors ***b*** are
696 5.512-8.649 and 3.115-4.003 for S2 and S13 cases respectively, verifying the quicker
697 decrease of $<P\_iF>_B$ in S13 cases. Moreover, double-layer lateral type (Case
698 [Lateral2_align or stagger, 30m, S2 or S13]) have the smallest decay factor b and the
699 quickest decrease processes of $<P\_iF>_B$ toward downstream regions.

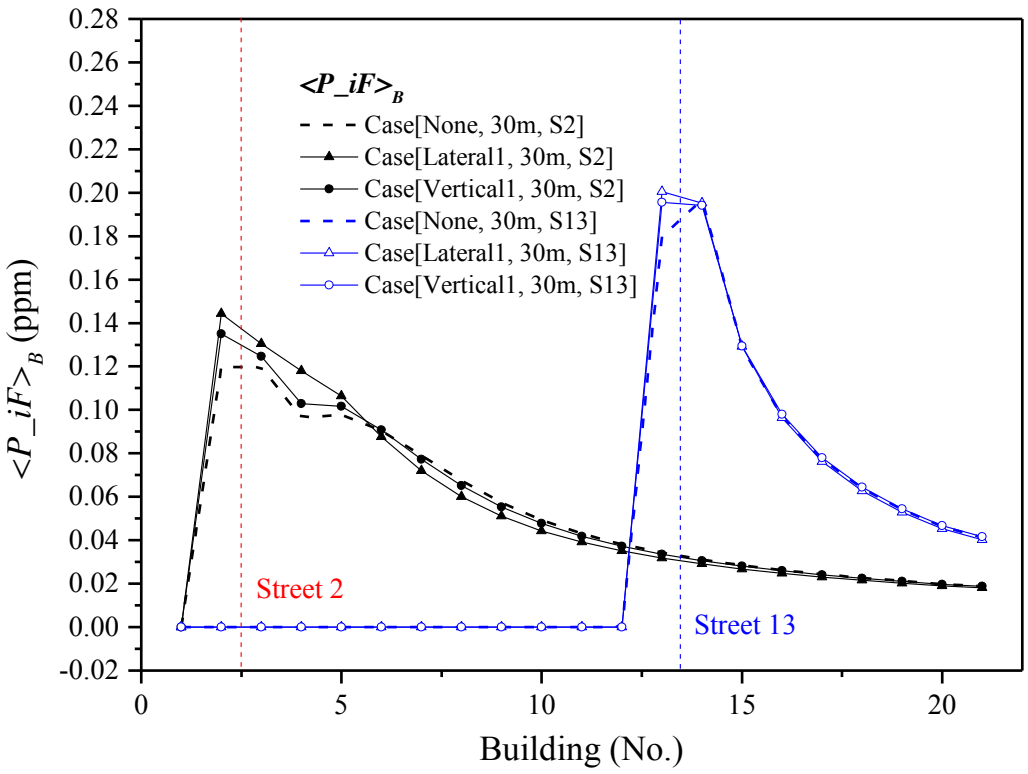
<P_iF>B
Case[None, 30m, S2]
Case[Lateral1, 30m, S2]
Case[Vertical1, 30m, S2]
Case[None, 30m, S13]
Case[Lateral1, 30m, S13]
Case[Vertical1, 30m, S13]
Street 2
Street 13
<P_iF>B (ppm)
Building (No.)

(a)

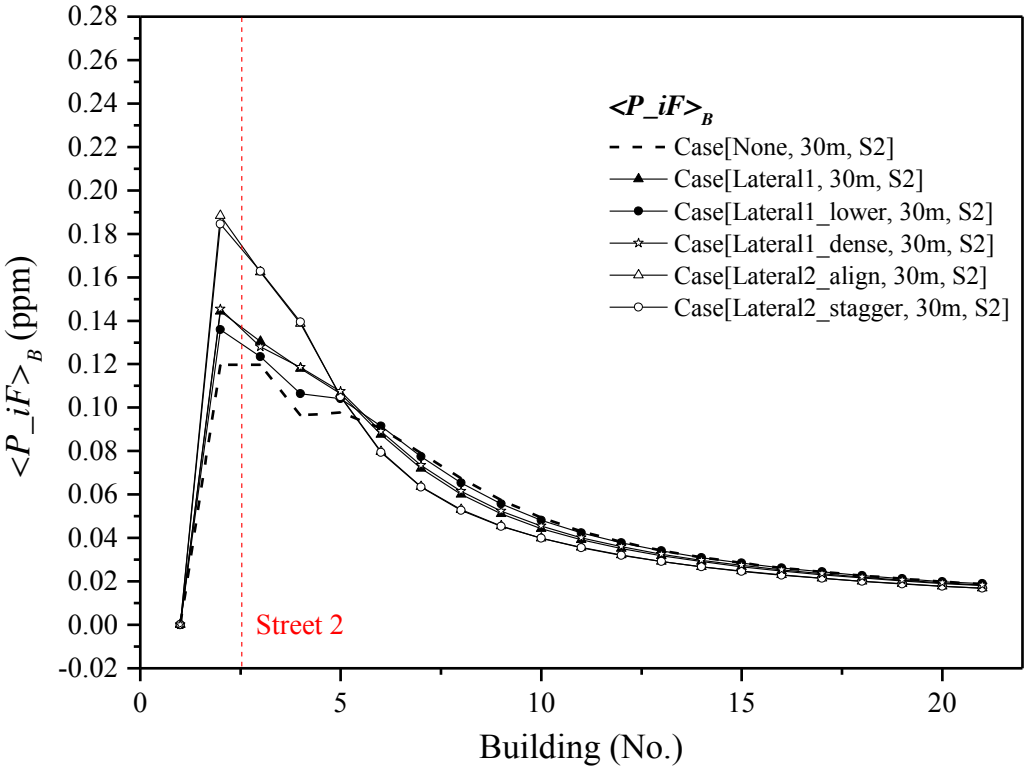
<P_iF>B
Case[None, 30m, S2]
Case[Lateral1, 30m, S2]
Case[Lateral1_lower, 30m, S2]
Case[Lateral1_dense, 30m, S2]
Case[Lateral2_align, 30m, S2]
Case[Lateral2_stagger, 30m, S2]
Street 2
<P_iF>B (ppm)
Building (No.)

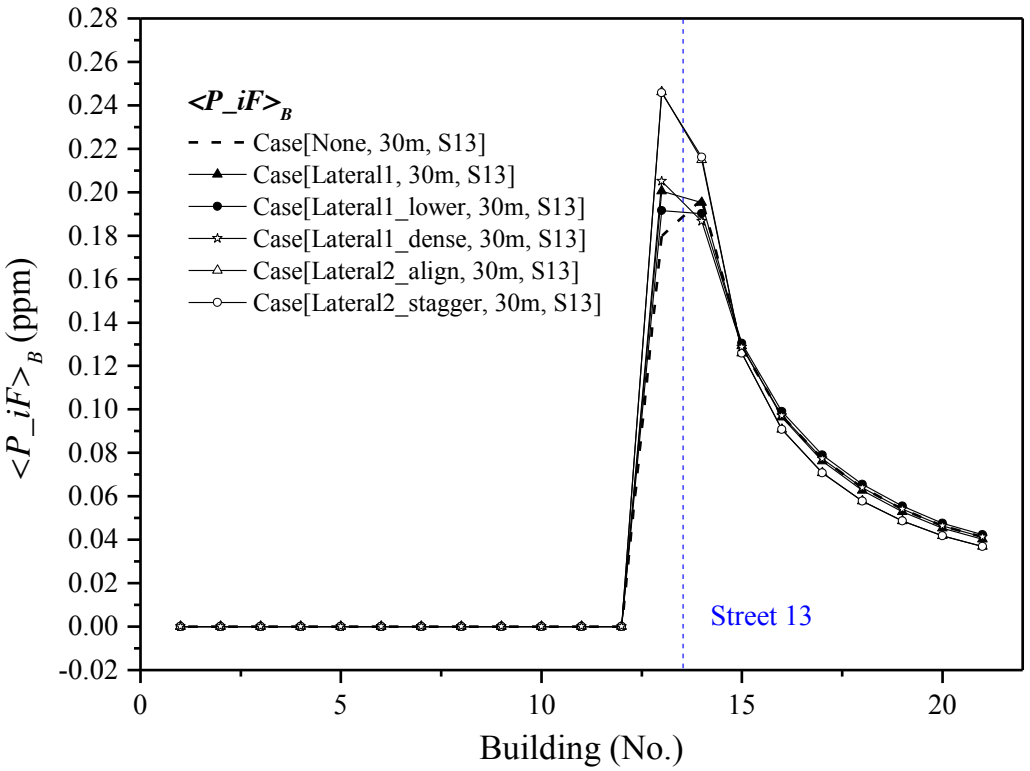

703
704

(b)

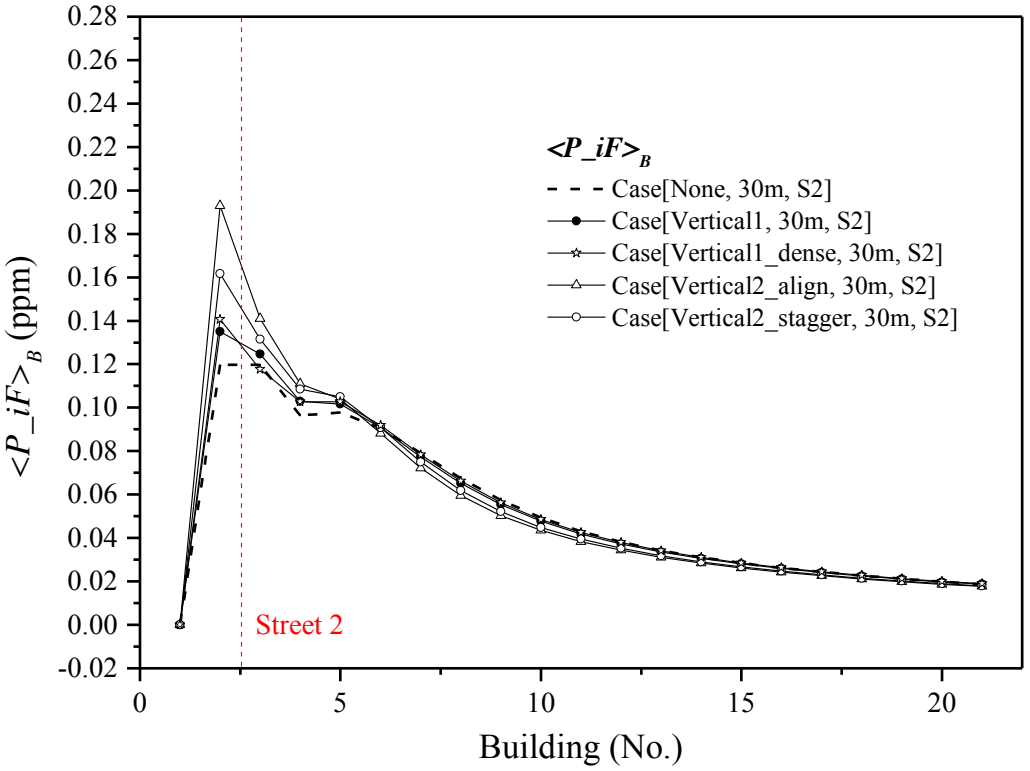

705
706

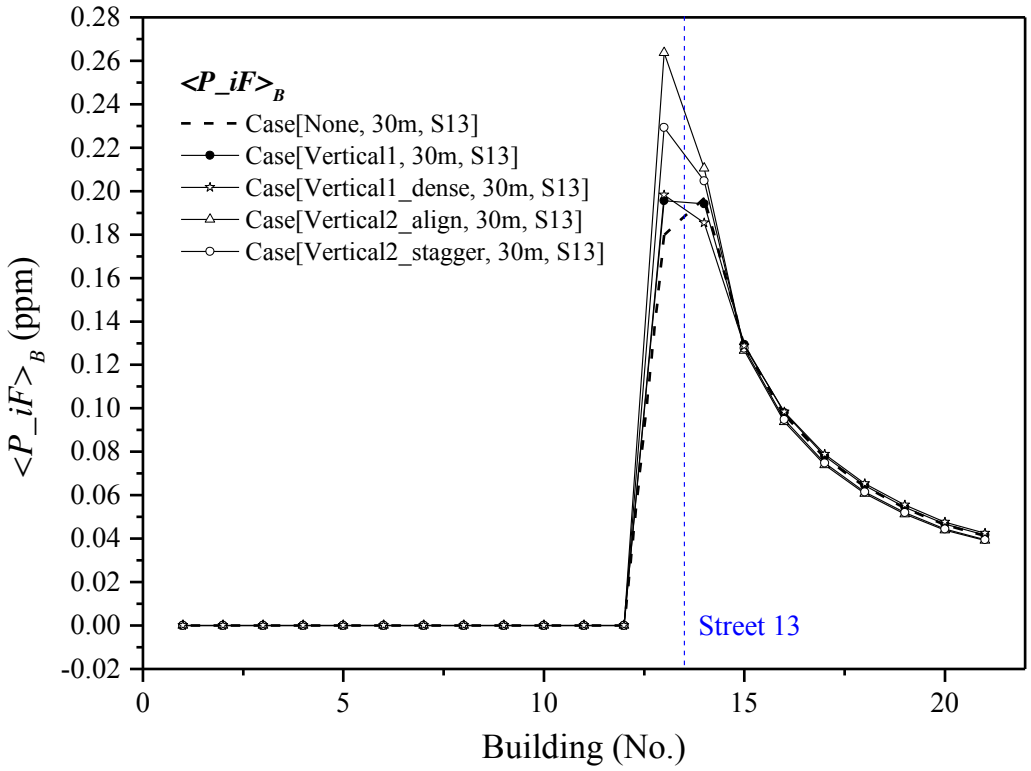

(c)

Fig. 14 $<P\_iF>_B$ profiles in example cases with 30m-wide secondary streets with CO source S2 or S13.

Table 5 Exponential decay factor ***b*** in $<P\_iF>_B$ decay profiles in cases with *Ws*=30m

Source	**S2**	**S13**
Case[None, 30m]	8.649	3.801
Case[Vertical1, 30m]	8.150	3.801
Case[Vertical1_dense, 30m]	8.487	3.510
Case[Vertical2_align, 30m]	6.970	3.887
Case[Vertical2_stagger, 30m]	7.439	3.367
Case[Lateral1, 30m,]	7.245	3.751
Case[Lateral1_dense, 30m]	7.443	4.003
Case[Lateral1_lower, 30m]	8.164	4.031
Case[Lateral2_align, 30m]	5.541	3.136
Case[Lateral2_stagger, 30m]	5.512	3.115

*Decay factor ***b*** calculated by fitting $<P\_iF_n>_B = a \times <P\_iF_{n_0}>_B \times e^{(n_0-n)/b}$, denotes $<P\_iF>_B$ decay rate from target street (n_0) toward downstream regions (For S2 and S13 cases n_0=3 and 14).

5.3 Impacts of advertisement boards on $\langle P\_iF \rangle_B$ in cases with Smain source

Fig. 15a-15b displays CO mass fraction (ppm) in the plane of z=1.5m (pedestrian level) with CO source along the main street (i.e. Smain) in cases with 30m-wide or 15m-wide secondary streets. Compared with cases without advertisement boards, all types of advertisement boards considerably raise CO concentration along the main street, and the lateral type seems to attain more CO exposure than vertical type. Fig. 15c-15e further shows $\langle P\_iF \rangle_B$ profiles toward downstream regions in Smain cases. For most 30m-wide cases (Fig. 15c-15d), $\langle P\_iF \rangle_B$ reaches an approximate equilibrium state at the 10th building for cases with single-layer types (Vertical1 and Lateral1) and at the 7th for double-layer types (i.e. shorter exposure adjustment distance). The equilibrium values of $\langle P\_iF \rangle_B$ with 30m-wide secondary streets are about 0.049-0.054ppm, much smaller than peak $\langle P\_iF \rangle_B$ in S2 or S13 cases with span-wise CO source (i.e. 0.12-0.26ppm in Fig. 14). Moreover, the double-layer types experience a little greater $\langle P\_iF \rangle_B$ than the single-layer types. These phenomena result from smaller in-canopy velocity induced by double-layer boards than the single-layer types. Finally, cases with 15m-wide secondary streets (Fig. 15e) attain longer adjustment distance for $\langle P\_iF \rangle_B$, and come to slightly greater equilibrium values of $\langle P\_iF \rangle_B$ (i.e. average 0.063ppm) than 30m-wide cases (0.049-0.054ppm). It can be explained that the 15m-wide secondary streets induce weaker drag force of buildings and smaller in-canopy velocity than 30m-wide secondary streets [32].

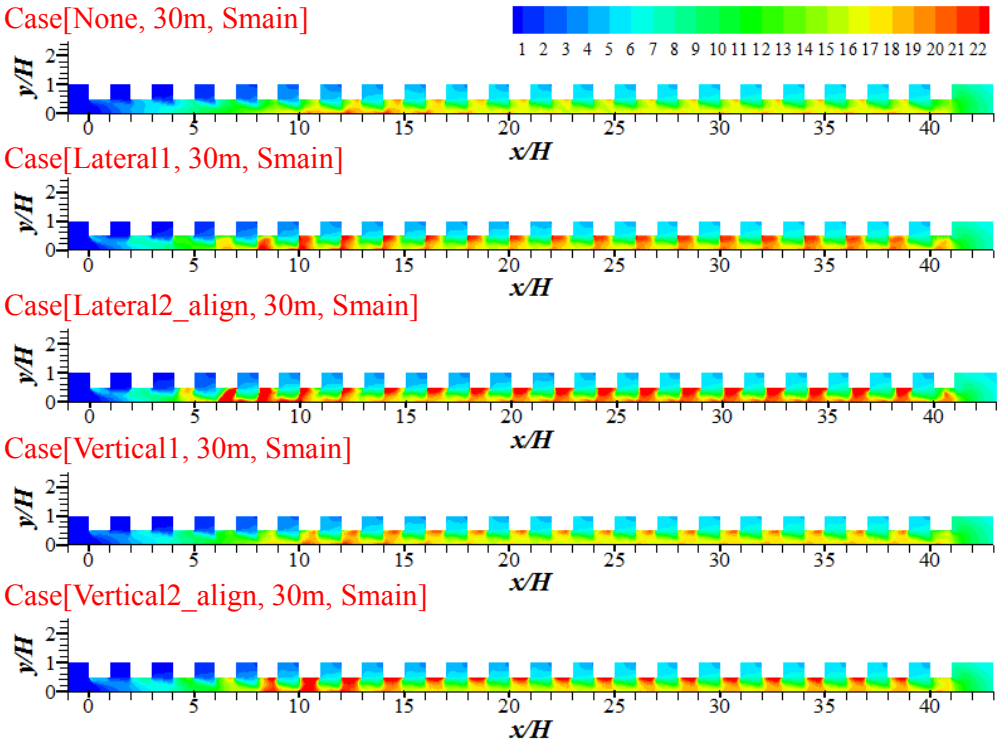
CO mass fraction (ppm) in plane of z=1.5m (pedestrian level)
Case[None, 30m, Smain]
1 2 3 4 5 6 7 8 9 10 11 12 13 14 15 16 17 18 19 20 21 22
y/H
x/H
Case[Lateral1, 30m, Smain]
Case[Lateral2_align, 30m, Smain]
Case[Vertical1, 30m, Smain]
Case[Vertical2_align, 30m, Smain]

(a)

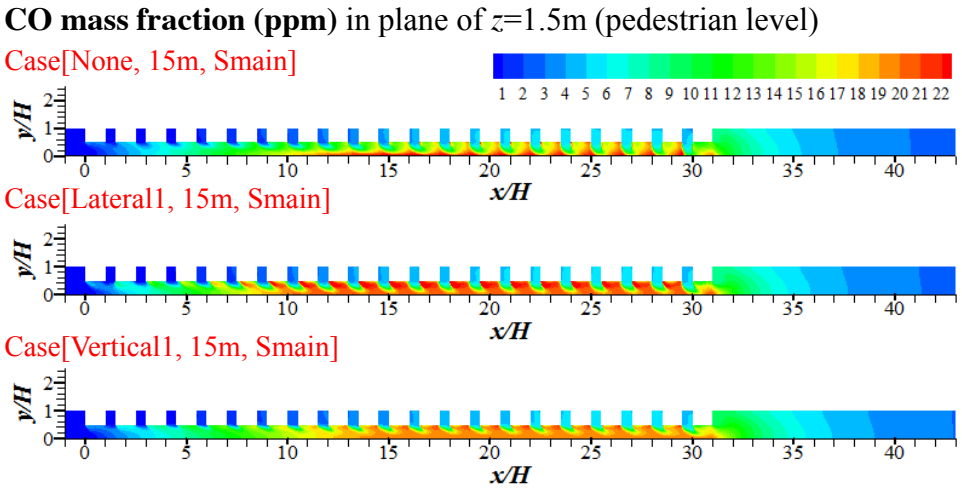
CO mass fraction (ppm) in plane of z=1.5m (pedestrian level)
Case[None, 15m, Smain]
1 2 3 4 5 6 7 8 9 10 11 12 13 14 15 16 17 18 19 20 21 22
y/H
x/H
Case[Lateral1, 15m, Smain]
Case[Vertical1, 15m, Smain]

(b)

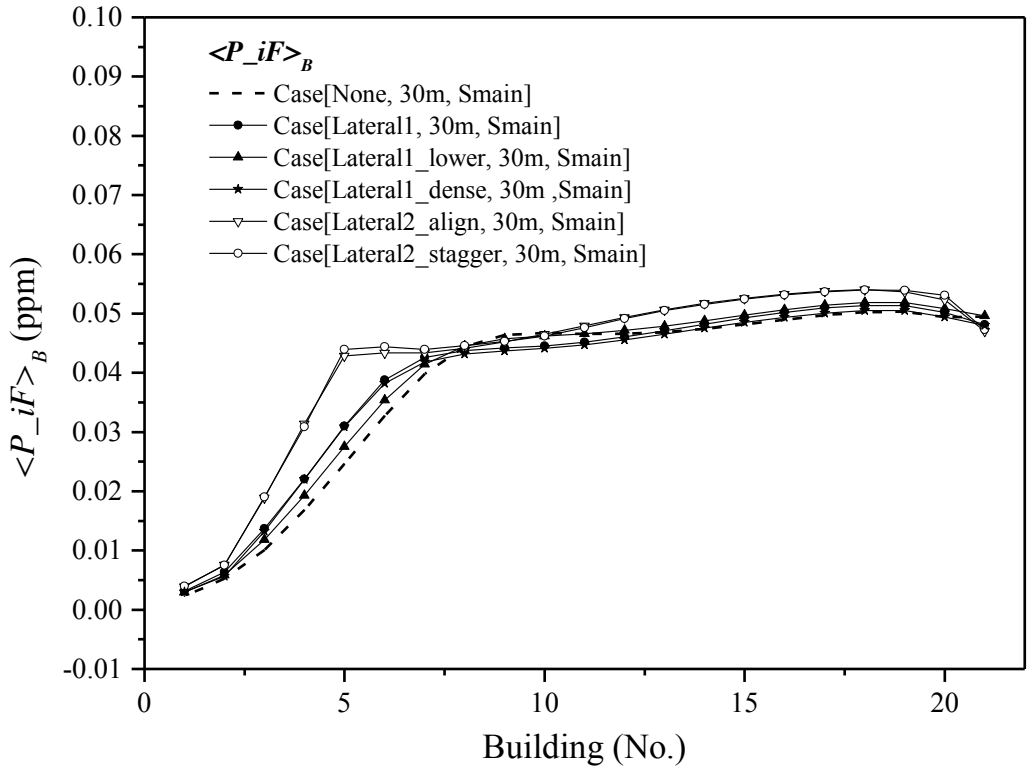

742

743 (c)

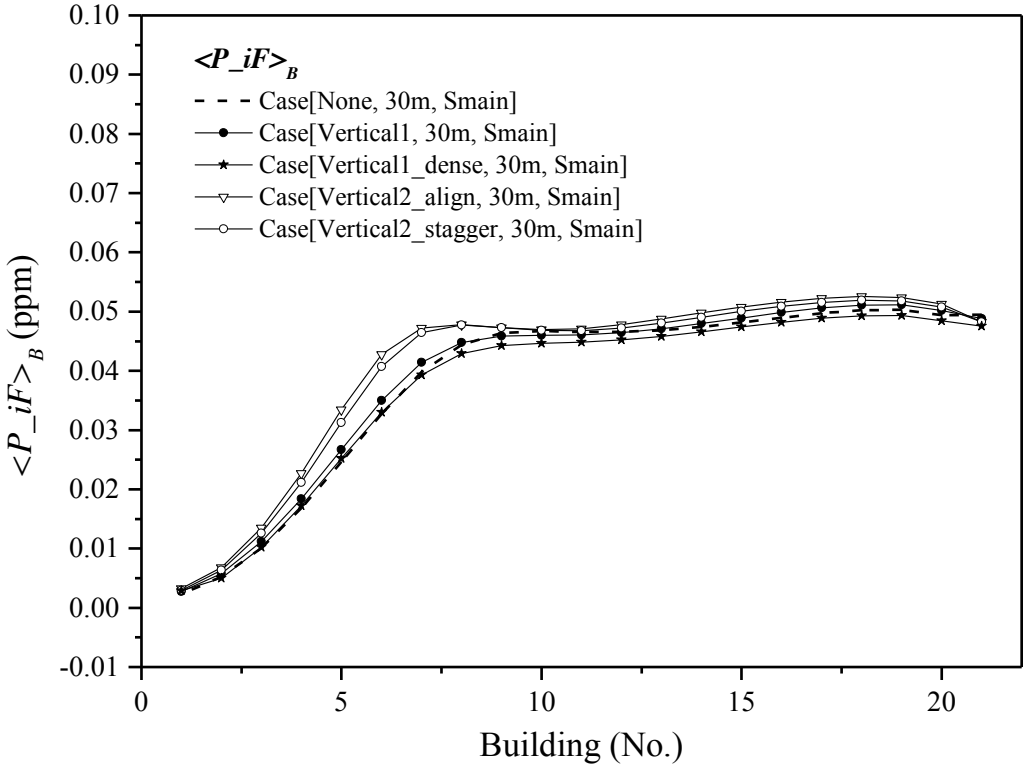

744

745 (d)

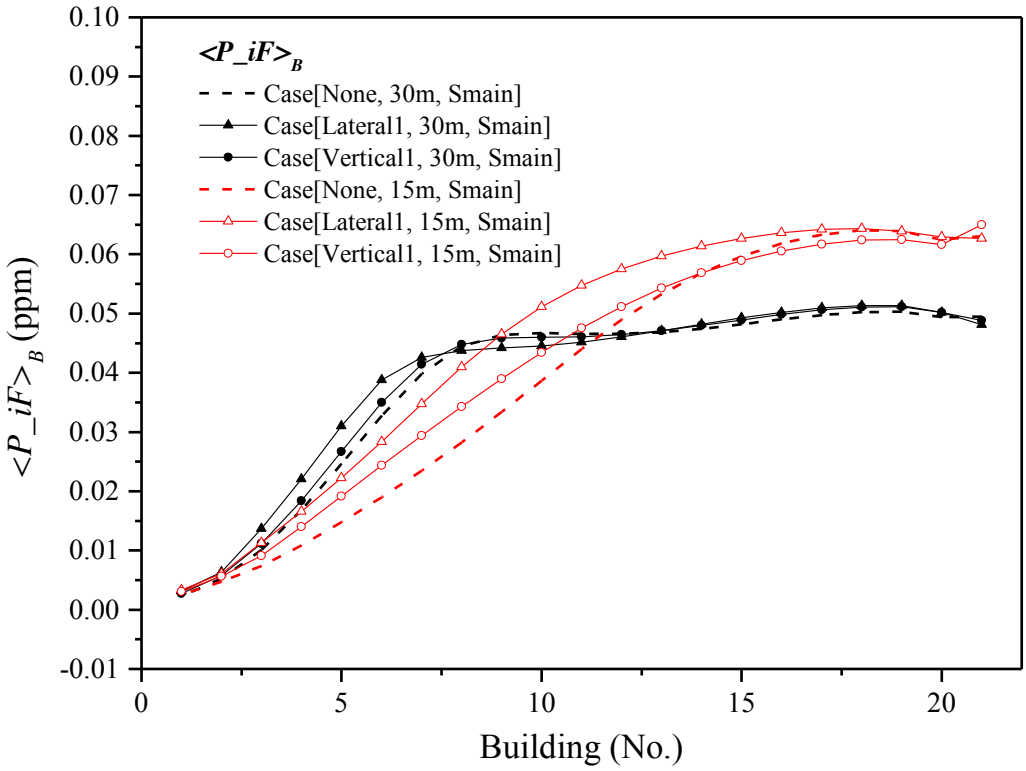

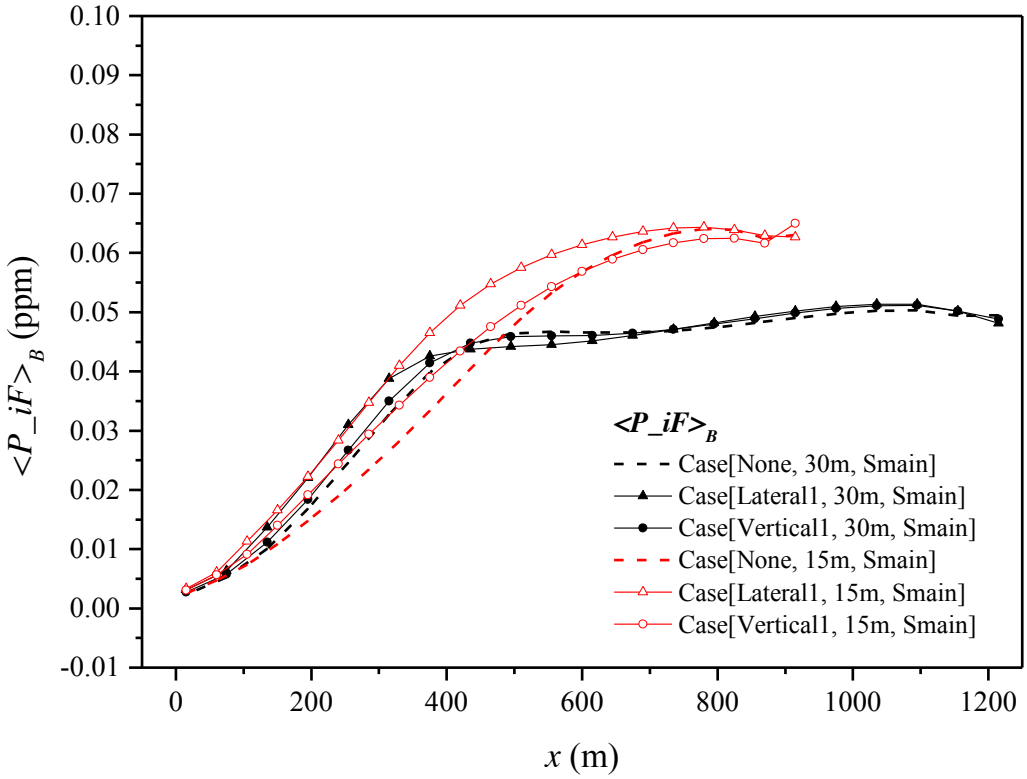

(e)

Fig.15 CO concentration in z=1.5m (pedestrian level) with CO source Smain in cases with (a) 30m-wide and (b) 15m-wide secondary streets. (c-e) $\langle P\_iF\rangle_B$ profiles in cases with CO source Smain.

752

753 **5.4 Limitations and future study**

754 Finally, it is worth mentioning that, as the urban models and advertisement board
755 models adopted here are fairly simplified and only residential buildings are
756 considered, the current exposure results possibly change if more realistic factors are
757 taken into account, such as more realistic urban morphologies, more complicated
758 advertisement boards and pollutant source settings, realistic atmospheric conditions
759 and various ambient wind directions, building air tightness and functions (residential,
760 commercial, industrial etc), pollutant properties (e.g. particle diameter) etc.
761 Furthermore, realistic meteorological conditions usually include the unsteady
762 temporal variations of wind speed and direction as well as various atmospheric
763 stabilities and relative importance of buoyancy force. Particularly, as confirmed by
764 outdoor field measurement (Mavroidis et al. [73]) and numerical simulation (Zhang et
765 al. [74]), urban airflow and pollutant dispersion under steady and unsteady boundary
766 conditions are different. For instance, Zhang et al. [74] reported that, unsteady wind
767 conditions experience lower pollutant concentration than that with unsteady
768 background wind and the same average wind speed.

769 Therefore, it still requires further investigations to perform unsteady CFD
770 simulations evaluated by the high-quality scale-model outdoor field measurement. For
771 this purpose, we developed a 3D building cluster (Fig. A2) consisting of more than
772 3000 concrete building models (building height H=1.2m, building width B=0.5m,
773 street width W=0.5m, H/W=2.4) in the suburb of Guangzhou for scale-model outdoor

774 measurement of urban micro-climate and health (SOMUCH). The unsteady velocity
775 and turbulence profiles, radiation characteristics, air and wall temperature within and
776 above the urban model were measured by using twenty ultrasonic anemometers, three
777 CRN4 radiometers, forty temperature and humidity sensors, two infrared cameras etc.
778 In recent future, the concentration distribution of tracer gas at 24 sites will be
779 measured with line source of tracer gas fixed near street ground. Further transient
780 numerical simulations will be conducted under the validation of scale-model outdoor
781 experimental data to investigate unsteady urban turbulence, pollutant dispersion and
782 personal exposure analysis in urban-like models.
783
784 **6 Conclusions**
785 Heavy traffic flows in street networks commonly result in serious urban air
786 pollution. Urban pollutant dispersion and their exposure assessment have become an
787 important issue. In particular, urban residents in near-road buildings commonly
788 experience high exposure risks to vehicular pollutants induced by street traffic flows.
789 Personal intake fraction (*P_iF*) represents the fraction of total CO emissions inhaled
790 by each person on average of a population. Particularly, building intake fraction
791 ($<P\_iF>_B$) denotes spatial mean *P_iF* for all floors of each building. Street layouts
792 and pollutant source settings are key influencing factors. Advertisement boards may
793 weaken urban windiness and raise pollutant exposure. Therefore, this paper
794 numerically quantify the integrated impacts of street aspect ratios (*H*/*Ws*=1 or 2), CO
795 source locations and advertisement boards on the flow, pollutant dispersion, $<P\_iF>_B$

796 in 3D urban-like models, which are still unclear so far. Neutral atmospheric condition
797 is first considered with the approaching wind parallel to the main street and
798 perpendicular to the secondary streets.

799 The aspect ratio of the secondary streets (H/Ws=1, 2; H=30m) and CO source
800 locations (span-wise and stream-wise type) are confirmed key factors. If the target
801 secondary street of No 2 or No 13 is fixed with CO source (i.e. span-wise CO source
802 S2 or S13), 3D downward helical flows transport more pollutants to the leeward side
803 in wider secondary streets (i.e. Ws=30m, H/Ws=1), inducing much greater
804 leeward-side $<P\_iF>$ than the windward-side. But it is opposite for cases with
805 narrower secondary streets (i.e. Ws=15m, H/Ws=2) in which windward-side $<P\_iF>$
806 is larger. It can be confirmed by the ratio of windward-side $<P\_iF>$ to leeward-side
807 $<P\_iF>$, i.e. $<P\_iF>_{lee/wind}$ is 3.710-4.701 as H/Ws=1 and 0.339-0.931 as H/Ws=2.
808 Moreover, H/Ws=2 experiences more limited upward CO dispersion, much greater
809 P_iF at low levels and smaller P_iF at high levels than H/Ws=1, thus the overall
810 average P_iF of both windward and leeward wall of the target street ($<P\_iF>_T$) as
811 H/Ws=2 (0.155-0.339ppm) is nearly half of that as H/Ws=1 (0.375-0.731ppm). There
812 are different findings for 2D street canyon model that $<P\_iF>_T$ (4.42ppm) as H/Ws=1
813 is smaller than that as H/Ws=2 (5.64ppm) which are one order greater than present 3D
814 urban models. Building intake fraction $<P\_iF>_B$ decreases exponentially from the
815 target street toward downstream. As span-wise CO source is fixed in the secondary
816 street, S13 attains greater $<P\_iF>_B$ and much larger decreasing rate toward
817 downstream than S2. Such exponential decay function is defined as

818 $< P\_iF_n >_B = a \times < P\_iF_{n_0} >_B \times e^{(n_0 - n)/b}$ (n=building number; n_0=3 and 14 for S2 and
819 S13 cases), and the decay factor ***b*** is 5.51-8.65 for S2 cases, and 3.12-4.00 for S13
820 cases, for which smaller ***b*** indicates $<P\_iF>_B$ decreases more quickly toward the
821 downstream. For cases with CO source in the main street parallel to the approaching
822 wind (i.e. stream-wise source, Smain), $<P\_iF>_B$ first rises quickly as deeper into
823 urban models, then increases slowly to the equilibrium values, which are 0.051ppm
824 and 0.063ppm as H/Ws=1 and 2 respectively, being only 20%-50% of the maximum
825 $<P\_iF>_B$ in cases with span-wise source S2 or S13 (i.e. 0.12-0.26ppm).
826 Advertisement boards are verified to slightly slow down 3D helical flow and
827 pollutant dispersion in the secondary streets, and such impact is more considerable
828 near building wall surfaces. All types of advertisement boards reduce urban wind
829 speed, enhance upward pollutant transportation and subsequently raise $<P\_iF>$ more
830 or less. With span-wise S2 or S13 source, advertisement boards produce greater
831 decreasing rates of $<P\_iF>_B$ towards downstream due to more pollutant stagnated in
832 the target secondary street. For a single building, vertical type and double-layer type
833 of advertisement boards produce stronger upward pollutant transportation and greater
834 $<P\_iF>_B$ than lateral type and single-layer ones. With stream-wise Smain source,
835 advertisement boards produce more surface roughness on the building walls, which
836 weaken the pollutant dilution and bring higher CO concentration near the building
837 row. In such cases, the double-layer and lateral types of advertisement boards produce
838 greater equilibrium values of $<P\_iF>_B$ and shorter exposure adjustment distance
839 toward the constant $<P\_iF>_B$ region. In conclusion, the influence of advertisement

840 boards on the pollutant dispersion and exposure mostly depends on two factors—the
841 vertical dimension and span-wise stretch. The vertical dimension decides how far the
842 pollutant can be transport upward on the building facades, while the span-wise stretch
843 serves as roughness that deteriorates the pollutant purging efficiency.

844 Although further investigations are still required to provide practical guidelines,
845 this paper is one of the first attempts to quantify how advertisement board types, street
846 aspect ratios, span-wise or stream-wise CO source setting influence flow and pollutant
847 exposure in 3D urban models, which can provide effective methodologies and
848 meaningful references to urban planning.

849

850 **Acknowledgements**

851 This study was financially supported by the National Natural Science Foundation
852 of China (No 51478486) and National Natural Science Foundation--Outstanding
853 Youth Foundation (grant No. 41622502), by STINT (dnr CH2017-7271) and the
854 National Natural Science Foundation of China (51811530017), as well as Science and
855 Technology Program of Guangzhou, China (grant No. 201607010066 and
856 2014B020216003).

857

858 **Reference list**

859 [1] J. Fenger, Urban air quality. Atmos. Environ. 33 (1999), 4877-4900.

860 [2] B. Zhou, B. Zhao, X.F. Guo, R.J. Chen, H.D. Kan, Investigating the
861 geographical heterogeneity in PM10-mortality associations in the China Air

862 Pollution and Health Effects Study (CAPES): A potential role of indoor
863 exposure to PM10 of outdoor origin, Atmos. Environ. 75 (2013) 217-223.
864 [3] R.J. Chen, B. Zhou, H.D. Kan, B. Zhao, Associations of particulate air pollution
865 and daily mortality in 16 Chinese cities: An improved effect estimate after
866 accounting for the indoor exposure to particles of outdoor origin. Environ.
867 Pollut. 182 (2013), 278-282.
868 [4] W.J. Ji, B. Zhao, Estimating mortality derived from indoor exposure to particles
869 of outdoor origin. PLOS.ONE. 10 (2015) e0124238.
870 [5] C. Chen, B. Zhao, W.T. Zhou, X.Y. Jiang, Z.C. Tan, A methodology for
871 predicting particle penetration factor through cracks of windows and doors for
872 actual engineering application, Build. Environ. 47 (2012) 339-348.
873 [6] W. Ng, C. Chau, A modelling investigation of the impact of street and building
874 configurations on personal air pollutant exposure in isolated deep urban
875 canyons, Sci. Total. Environ. 468-469 (2014) 429-448.
876 [7] Y. Zhou, J.I. Levy, The impact of urban street canyons on population exposure
877 to traffic-related primary pollutants, Atmos. Environ. 42 (2008) 3087-3098.
878 [8] G. Habilomatis, A. Chaloulakou, A CFD modelling study in an urban street
879 canyon for ultrafine particles and population exposure: The intake fraction
880 approach, Sci. Total. Environ. 530-531 (2015) 227-232.
881 [9] J. Hang, Z.W. Luo, X.M. Wang, L.J. He, B.M. Wang, W. Zhu, The influence of
882 street layouts and viaduct settings on daily CO exposure and intake fraction in
883 idealized urban canyons, Environ. Pollut. 220 (2017) 72-86.

884 [10] L.J. He, J. Hang, X.M. Wang, B.R. Lin, X.H. Li, G.D. Lan, Numerical
885 investigations of flow and passive pollutant exposure in high-rise deep street
886 canyons with various street aspect ratios and viaduct settings, Sci. Total
887 Environ. 584-585 (2017) 189-206.
888 [11] R.E. Britter, S.R. Hanna, Flow and dispersion in urban areas, Annu. Rev. Fluid.
889 Mech. 35 (2003) 469-496.
890 [12] H.J.S. Fernando, D. Zajic, S. Di Sabatino, R. Dimitrova, B. Hedquist, Flow,
891 turbulence, and pollutant dispersion in urban atmospheres, Phys. Fluids. 22
892 (2010) 1-20.
893 [13] B. Blocken, CFD simulation of micro-scale pollutant dispersion in the built
894 environment, Build. Environ. 64 (2013) 225–230.
895 [14] K.G. Zhu, M. Xie, T.J. Wang, X.J. Cai, S.B. Li, W. Feng, A modeling study on
896 the effect of urban land surface forcing to regional meteorology and air quality
897 over South China, Atmos. Environ. 152(2017) 389-404.
898 [15] L. Shu, M. Xie, D. Gao, T. Wang, D. Fang, Q. Liu, A. Huang, L. Peng, Regional
899 severe particle pollution and its association with synoptic weather patterns in
900 the Yangtze River Delta region, China, Atmos. Chem. Phys. 17(2017)
901 12871-12891.
902 [16] Y. Tominaga, T. Stathopoulos, CFD simulation of near-field pollutant dispersion
903 in the urban environment: A review of current modeling techniques. Atmos.
904 Environ. 79 (2013) 716-730.
905 [17] B. Blocken, Computational fluid dynamics for urban physics: importance,

906 scales, possibilities, limitations and ten tips and tricks towards accurate and
907 reliable simulations, Build. Environ. 91 (2015) 219-245.
908 [18] R.N. Meroney, Ten questions concerning hybrid computational/physical model
909 simulation of wind flow in the built environment, Build. Environ. 96 (2016)
910 12-21.
911 [19] X.X. Li, C.H. Liu, D.Y.C. Leung, K.M. Lam, Recent progress in CFD
912 modelling of wind field and pollutant transport in street canyons, Atmos.
913 Environ. 40 (2006) 5640-5658.
914 [20] Y.W. Zhang, Z. Gu, W. Y. Chuck, Review on numerical simulation of airflow
915 and pollutant dispersion in urban street canyons under natural background wind
916 conditions. Aerosol. Air. Qual. Res. 18 (2018), 780-789.
917 [21] J. Hang, M. Sandberg, Y.G. Li. Age of air and air exchange efficiency in
918 idealized city models. Build. Environ. 44(8) (2009)1714-1723.
919 [22] T. van Hooff, B. Blocken, CFD evaluation of natural ventilation of indoor
920 environments by the concentration decay method: CO2 gas dispersion from a
921 semi-enclosed stadium, Build. Environ. 61 (2013) 1-17.
922 [23] J. Hang, Q. Wang, X.Y. Chen, M. Sandberg, W. Zhu, R. Buccolieri, S. Di
923 Sabatino, City breathability in medium density urban-like geometries evaluated
924 through the pollutant transport rate and the net escape velocity, Build. Environ.
925 94 (2015) 166-182.
926 [24] B. Blocken, R. Vervoort, T.A.J. van Hooff, Reduction of outdoor particulate
927 matter concentrations by local removal in semi-enclosed parking garages: a

928 preliminary case study for Eindhoven city center, J. Wind. Eng. Ind. Aerodyn.
929 159 (2016) 80-98.
930 [25] H.L Gough, Z. Luo, C.H. Halios, M.F. King, C.J. Noakes, C.S.B. Grimmond,
931 J.F. Barlow, R. Hoxey, A.D. Quinn, Field measurement of natural ventilation
932 rate in an idealised full-scale building located in a staggered urban array:
933 Comparison between tracer gas and pressure-based methods. Build. Environ.
934 137 (2018) 246-256.
935 [26] R.N Meroney, M. Pavageau, S. Rafailidis, M. Schatzmann, Study of line source
936 characteristics for 2-D physical modelling of pollutant dispersion in street
937 canyons, J. Wind. Eng. Ind. Aerodn. 62 (1996) 37-56.
938 [27] X.X. Li, C.H. Liu, D.Y.C. Leung, Large-eddy simulation of flow and pollutant
939 dispersion in high-aspect-ratio urban street canyons with wall model,
940 Bound-Lay. Meteorol. 129 (2008) 249-268.
941 [28] S.R. Hanna, S. Tehranian, B. Carissimo, R.W. Macdonald, R. Lohner.
942 Comparisons of model simulations with observations of mean flow and
943 turbulence within simple obstacle arrays. Atmos. Environ. 36 (2002)
944 5067-5079.
945 [29] C.H. Chang, R.N. Meroney, Concentration and flow distributions in urban street
946 canyons: wind tunnel and computational data, J. Wind. Eng. Ind. Aerodn. 91
947 (2003) 1141-1154.
948 [30] R. Ramponi, B. Blocken, L.B. de Coo, W.D. Janssen, CFD simulation of
949 outdoor ventilation of generic urban configurations with different urban

densities and equal and unequal street widths, Build. Environ. 92 (2015) 152-166.

[31] R. Buccolieri, M. Sandberg, S. Di Sabatino, City breathability and its link to pollutant concentration distribution within urban-like geometries, Atmos. Environ. 44 (2010) 1894-1903.

[32] J. Hang, Y.G. Li, Age of air and air exchange efficiency in high-rise urban areas and its link to pollutant dilution, Atmos. Environ. 45 (2011) 5572-5585.

[33] M. Lin, J. Hang, Y.G. Li, Z.W. Luo, M. Sandberg, Quantitative ventilation assessments of idealized urban canopy layers with various urban layouts and the same building packing density, Build. Environ. 79 (2014) 152-167.

[34] Z.L. Gu, Y.W. Zhang, Y. Cheng, S.C. Lee, Effect of uneven building layout on airflow and pollutant dispersion in non-uniform street canyons, Build. Environ. 46 (2011) 2657-2665.

[35] Y.X. Du, C.M. Mak, J.L. Liu, Q. Xia, J.L. Niu, K.C.S. Kwok, Effects of lift-up design on pedestrian level wind comfort in different building configurations under three wind directions, Build. Environ. 117 (2017) 84-99.

[36] J.L. Liu, J.L. Niu, C.M. Mak, Q. Xia, Detached eddy simulation of pedestrian-level wind and gust around an elevated building, Build. Environ. 125 (2017) 168-179.

[37] C.Y. Sha, X.M. Wang, Y.Y. Lin, Y.F. Fan, X. Chen, J. Hang, The impact of urban open space and 'lift-up' building design on building intake fraction and

971 daily pollutant exposure in idealized urban models. Sci. Total. Environ. 633
972 (2018) 1314-1328.
973 [38] J. Hang, Z.N. Xian, D.Y. Wang, C.M. Mak, B.M. Wang, Y.F. Fan,The impacts
974 of viaduct settings and street aspect ratios on personal intake fraction in
975 three-dimensional urban-like geometries, Build. Environ. 143(2018) 138-162.
976 [39] C. Gromke, B. Blocken, Influence of avenue-trees on air quality at the urban
977 neighborhood scale. Part I: Quality assurance studies and turbulent Schmidt
978 number analysis for RANS CFD simulations, Environ. Pollut. 196 (2015)
979 214-223.
980 [40] C. Gromke, B. Blocken, Influence of avenue-trees on air quality at the urban
981 neighborhood scale. Part II: Traffic pollutant concentrations at pedestrian level,
982 Environ. Pollut. 196 (2015) 176-184.
983 [41] C.H. Wang, Q. Li, Z.H. Wang. Quantifying the impact of urban trees on passive
984 pollutant dispersion using a coupled large-eddy simulation–Lagrangian
985 stochastic model. Build. Environ 145 (2018) 33-49.
986 [42] Y.W. Zhang, Z.L. Gu, C.W. Yu, Large eddy simulation of vehicle induced
987 turbulence in an urban street canyon with a new dynamically vehicle-tracking
988 scheme. Aerosol. Air. Qual. Res. 17(3) (2017) 865-874.
989 [43] N. Nazarian, J.Kleissl, Realistic solar heating in urban areas: Air exchange and
990 street-canyon ventilation, Build. Environ. 95 (2016) 75-93.

991 [44] Y. Toparlar, B. Blocken, P. Vos, G.J.F. van Heijst, W.D. Janssen, H. Montazeri,
992 H.J.P. Timmermans, CFD simulation and validation of urban microclimate: A
993 case study for Bergpolder Zuid, Rotterdam. Build. Environ. 83 (2015) 79-90.
994 [45] X.Y. Yang, Y.G. Li, The impact of building density and building height
995 heterogeneity on average urban albedo and street surface temperature, Build.
996 Environ. 90 (2015) 146-156.
997 [46] P.Y. Cui, Z. Li, W.Q. Tao, Buoyancy flows and pollutant dispersion through
998 different scale urban areas: CFD simulations and wind-tunnel measurements,
999 Build. Environ. 104 (2016) 76-91.
1000 [47] X.X. Wang, Y.G. Li, Predicting urban heat island circulation using CFD, Build.
1001 Environ. 99 (2016) 82-97.
1002 [48] Y.F. Fan, J.C.R. Hunt, Y.G. Li, Buoyancy and turbulence-driven atmospheric
1003 circulation over urban areas, J. Environ. Sci. 59 (2017) 63-71.
1004 [49] X.X. Li, R.E. Britter, L.K. Norford, Effect of stable stratification on dispersion
1005 within urban street canyons: A large-eddy simulation, Atmos. Environ. 144
1006 (2016) 47-59.
1007 [50] X. M. Cai, Effects of differential wall heating in street canyons on dispersion
1008 and ventilation characteristics of a passive scalar, Atmos. Environ. 51 (2012)
1009 268-277.
1010 [51] L. Lin, J. Hang, X.X. Wang, X.M. Wang, S.J. Fan, Q. Fan, Y.H. Liu, Integrated
1011 effects of street layouts and wall heating on vehicular pollutant dispersion and

1012 their reentry into downstream canyons, Aerosol Air Qual. Res. 16 (2016) 3142-
1013 3163.
1014 [52] J. Liu, Z.W. Luo, J.N. Zhao, T.Y. Shui. Ventilation in a street canyon under
1015 diurnal heating conditions. Int. J. Vent.,11(2) (2012). 141-154.
1016 [53] J.Y. Liu, J. Srebric, N.Y. Yu, Numerical simulation of convective heat transfer
1017 coefficient at the external surfaces of building arrays immersed in a turbulent
1018 boundary layer, Inter. J. Heat. Mass. Trans. 61 (2013) 209-225.
1019 [54] W.W. Wang, E. Ng, Air ventilation assessment under unstable atmospheric
1020 stratification - A comparative study for Hong Kong, Build. Environ. 130(2018)
1021 1-13.
1022 [55] M. Kalaiarasan, R. Balasubramanian, K.W.D. Cheong, K.W. Tham,
1023 Traffic-generated airborne particles in naturally ventilated multi-storey
1024 residential buildings of Singapore: Vertical distribution and potential health risks,
1025 Build. Environ. 44.7 (2009) 1493-1500.
1026 [56] Z.W. Luo, Y.G. Li, W.W. Nazaroff, Intake fraction of nonreactive motor
1027 vehicle exhaust in Hong Kong, Atmos. Environ. 44 (2010) 1913-1918.
1028 [57] C.K. Chau, E.Y. Tu, D.W.T. Chan, C.J. Burnett, Estimating the total exposure
1029 to air pollutants for different population age groups in Hong Kong, Environ.
1030 Inter. 27 (2002) 617-630.
1031 [58] M. Allan, G.M. Richardson, H. Jones-Otazo, Probability density functions
1032 describing 24-hour inhalation rates for use in human health risk assessments: an
1033 update and comparison, Hum. Ecol. Risk. Assess. 14 (2008) 372-391.

[59] T.N. Quang, C. He, L. Morawska, L.D. Knibbs, M. Falk, Vertical particle concentration profiles around urban office buildings, Atmos. Chem. Phys. 12 (2012) 5017-5030.

[60] R. Yoshie, A. Mochida, Y. Tominaga, T. Shirasawa. Cooperative project for CFD prediction of pedestrian wind environment in the Architectural Institute of Japan, J. Wind. Eng. Ind. Aerodyn. 95(2007) 1551-1578.

[61] FLUENT V6.3, http://fluent.com. Accessed in 2006.

[62] M.J. Brown, R.E. Lawson, D.S. DeCroix, R. L. Lee, Comparison of centerline velocity measurements obtained around 2D and 3D building arrays in a wind tunnel. Report LA-UR-01-4138, Los Alamos National Laboratory, Los Alamos, (2001) pp.7.

[63] F.S. Lien, E. Yee, Numerical modeling of the turbulent flow developing within and over a 3-D building array, part I: A high-resolution Reynolds-averaged Navier-Stokers approach, Bound-lay. Meteorol. 112 (2004) 427-466.

[64] J. Hang, Y.G. Li, Wind conditions in idealized building clusters – macroscopic simulations using a porous turbulence model. Boundary-Lay. Meteorol. 136(1) (2010) 129-159.

[65] J.L. Santiago, A. Martilli, F. Martin, CFD simulation of airflow over a regular array of cubes. Part I: three dimensional simulation of the flow and validation with wind-tunnel measurements, Bound-lay. Meteorol. 122 (2007) 609-634.

1054 [66] J.S. Irwin, A theoretical variation of the wind profile power-law exponent as a
1055 function of surface roughness and stability, Atmos. Environ. 13(1) (1979) 191-
1056 194.
1057 [67] Y. Tominaga, A. Mochida, R. Yoshie, H. Kataoka, T. Nozu, M. Yoshikawa, T.
1058 Shirasawa, AIJ guidelines for practical applications of CFD to pedestrian wind
1059 environment around buildings, J. Wind. Eng. Ind. Aerod. 96 (2008) 1749-1761.
1060 [68] J. Franke, A. Hellsten, H. Schlunzen, B. Carissimo, The COST732 Best Practice
1061 Guideline for CFD simulation of flows in the urban environment a summary, Int.
1062 J. Environ. Pollut. 44 (2011) 419-427.
1063 [69] W.H. Snyder, Similarity criteria for the application of fluid models to the study
1064 of air pollution meteorology. Bound-Lay. Meteorol. 3(1972) 113-134.
1065 [70] S. Di Sabatino, R. Buccolieri, H.R. Olesen, M. Ketzel, R. Berkowicz, J. Franke,
1066 M. Schatzmann, K.H. Schlunzen, B. Leitl, R. Britter, C. Borrego, A.M. Costa, A.
1067 Trini Castelli, T.G. Reisin, A. Hellsten, J. Saloranta, N. Moussiopoulos, F.
1068 Barmpas, K. Brzozowski, I. Goricsan, M. Balczo, J.G. Bartzis, G. Efthimiou, J.L.
1069 Santiago, A. Martilli, M. Piringer, K. Baumann-Stanzer, M. Hirtl, A.A. Baklanov,
1070 R.B. Nuterman, A.V. Starchenko, COST 732 in practice: the MUST model
1071 evaluation exercise, Int. J. Env. Poll. 44(2011) 1-4.
1072 [71] K. Schlünzen, W. Bächlin, H. Brünger, J. Eichhorn, D. Grawe, R. Schenk, C.
1073 Winkler, 9th international conference on harmonisation within atmospheric
1074 dispersion modelling for regulatory purposes, Garmisch-Partenkirchen, June
1075 2004: 1-4.

[72] C.H. Chang, R.N. Meroney, Numerical and physical modeling of bluff body flow and dispersion in urban street canyons, Wind Eng. Ind. Aerodyn. 89.14-15 (2001) 1325-1334.

[73] I. Mavroidis, R.F. Griffiths, Local characteristics of atmospheric dispersion within building arrays. Atmos. Environ. 35 (2001) 2941-2954.

[74] Y.W. Zhang, Z. Gu, Y. Cheng, S.C. Lee, Effect of real-time boundary wind conditions on the air flow and pollutant dispersion in an urban street canyon Large eddy simulations. Atmos. Environ. 45(2011) 3352-3359.

Appendix

As Brown et al. [62] did not present the measurement result at the street side (i.e. along the main street parallel to the approaching wind), as depicted in Fig. A1, the data of another wind tunnel experiment was adopted to verify the effectiveness of the "half column method" in the street side.

The experiment was carried out in the wind tunnel laboratory at the University of Gavle, Sweden (Fig. A1a). An idealized 1:200 scaled urban model containing 27 rows and 15 columns of evenly separated cuboids (B=W=5cm, H=12cm) was built (Fig. A1b). Velocities were measured using Laser Doppler Anemometer system. The reference velocity of parallel coming wind (i.e. U_{ref}, Stream-wise velocity u at z=H) was 1.67m/s, with a large enough reference Re value as 1.39×10^4 at building height (z=H=12cm), which met the Re independence criterion [69]. The x, y and z direction were defined as the stream-wise, span-wise and vertical direction separately.

A full-scale CFD model with half of the middle column and street was established for validation study (Fig. A1c). The velocity and TKE profiles measured in that experiment were applied for the inlet condition (Fig. A1d). And the vertical profile of inlet TED ($\varepsilon(z)$) was calculated by Eq. (12). Same boundary conditions as the validation cases described in subsections 4.1 were adopted at domain outlet, domain top and lateral boundaries (Fig. A1c). Moreover, the urban model is 53H long, while the urban boundaries are 9H from the domain roof, 6.3H from the inlet, and 41.7H from the domain outlet. Grid independence was also studied. Three different grid arrangements were tested: fine grid arrangement (the minimum grid size next to the wall surface was 0.1m, about 4.4 million hexahedral cells in total), medium grid arrangement (minimum grid size of 0.2m, about 2.2 million cells), and coarse grid arrangement (minimum grid size of 0.4m, about 0.9 million cells). Fig. A1e displays the CFD results of normalized stream-wise velocity profile (i.e. $\bar{u}(z)/U_{ref}$, $U_{ref}=U_{z=H}$ of wind tunnel experiment) at the center of cross street at x/H=25.5 (point S1). It shows that standard k-ε model performed well and there was little difference between the prediction results using fine or medium grid arrangement. The result also convinced that the "half column method" with present CFD methodologies applied is reliable for such urban flow simulation studied in this paper.

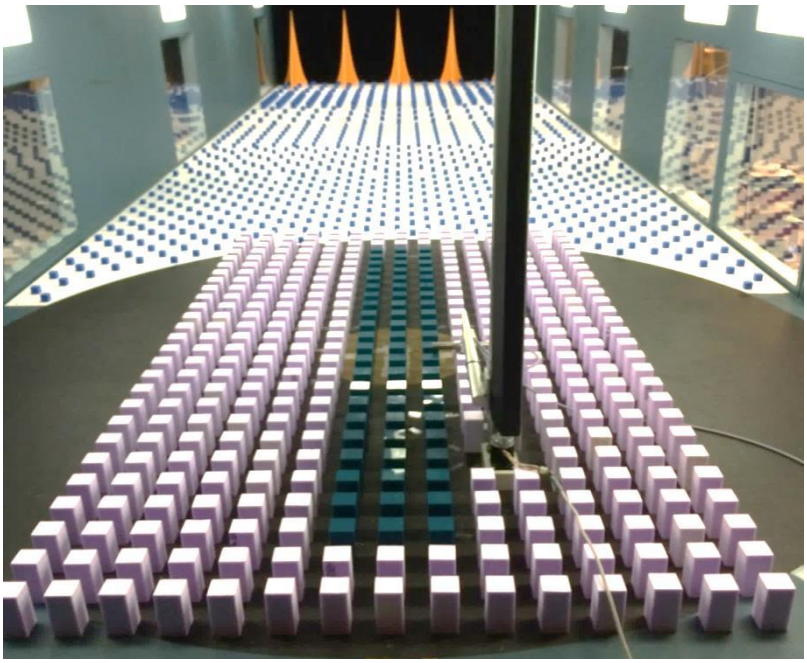

(a)

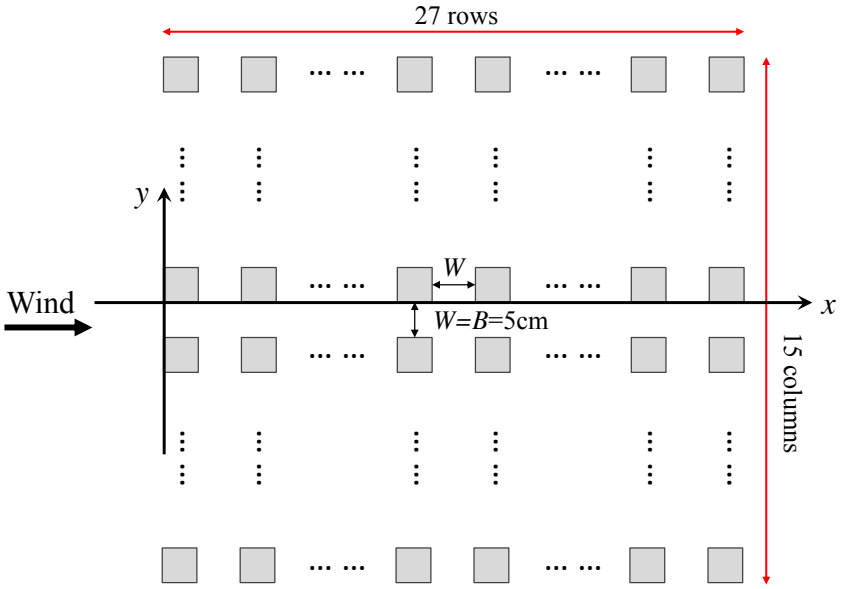
27 rows
y
Wind
W
W=B=5cm
x
15 columns

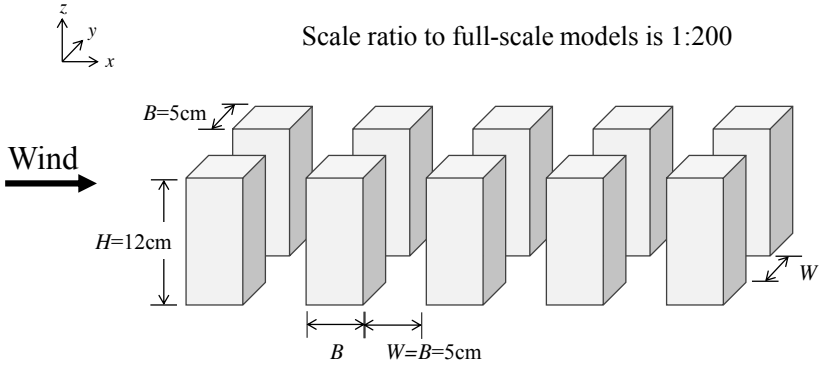
z
y
x
Scale ratio to full-scale models is 1:200
B=5cm
Wind
H=12cm
W
B
W=B=5cm

(b)

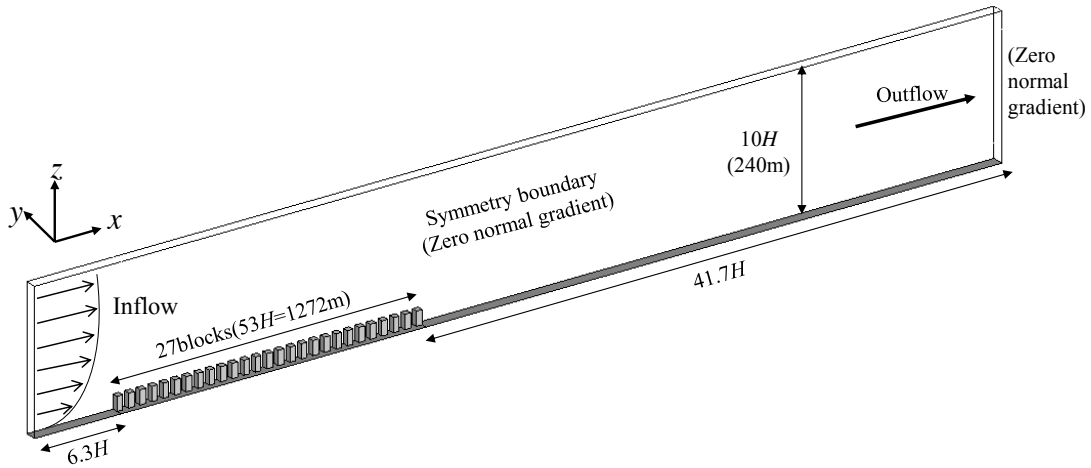
z
y
x
Inflow
27blocks(53H=1272m)
6.3H
Symmetry boundary
(Zero normal gradient)
10H
(240m)
41.7H
Outflow
(Zero
normal
gradient)

(c)

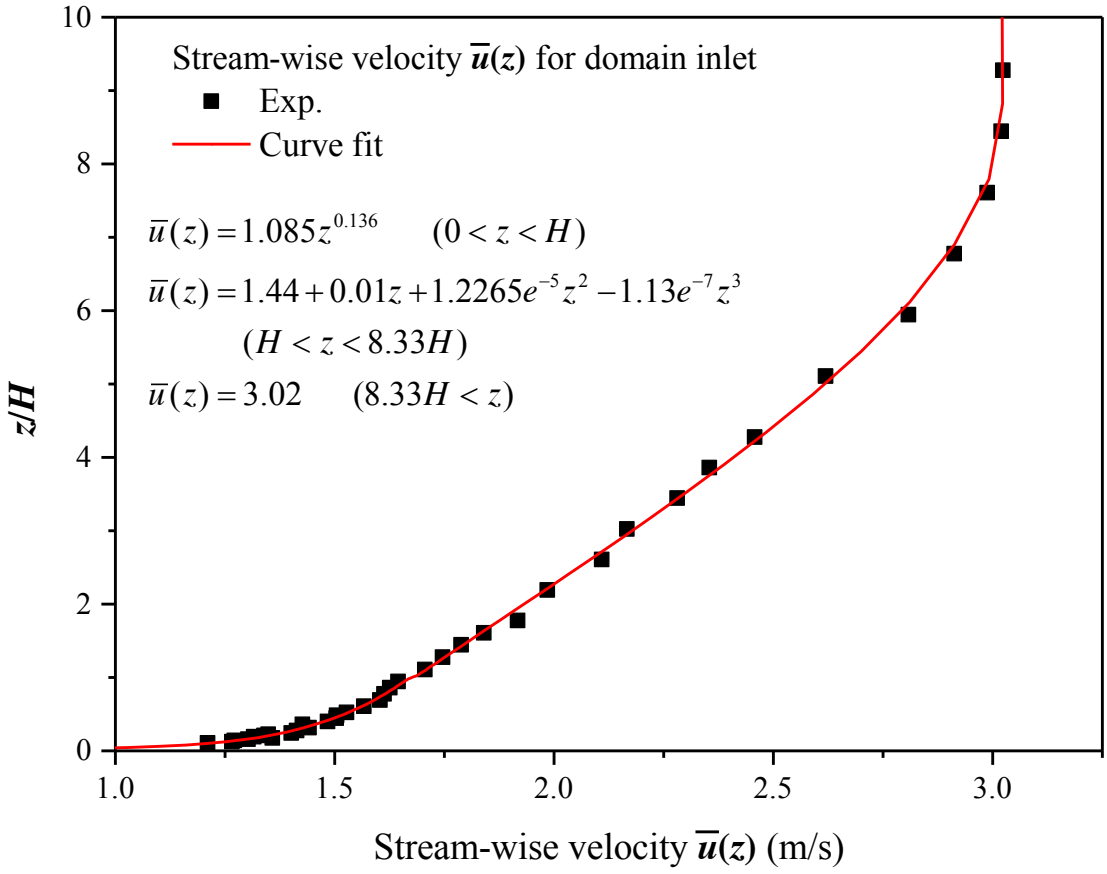
Stream-wise velocity $\overline{u}(z)$ for domain inlet
Exp.
Curve fit
$\overline{u}(z) = 1.085z^{0.136}$ $(0 < z < H)$
$\overline{u}(z) = 1.44 + 0.01z + 1.2265e^{-5}z^2 - 1.13e^{-7}z^3$
$(H < z < 8.33H)$
$\overline{u}(z) = 3.02$ $(8.33H < z)$
z/H
Stream-wise velocity $\overline{u}(z)$ (m/s)
0
2
4
6
8
10
1.0
1.5
2.0
2.5
3.0

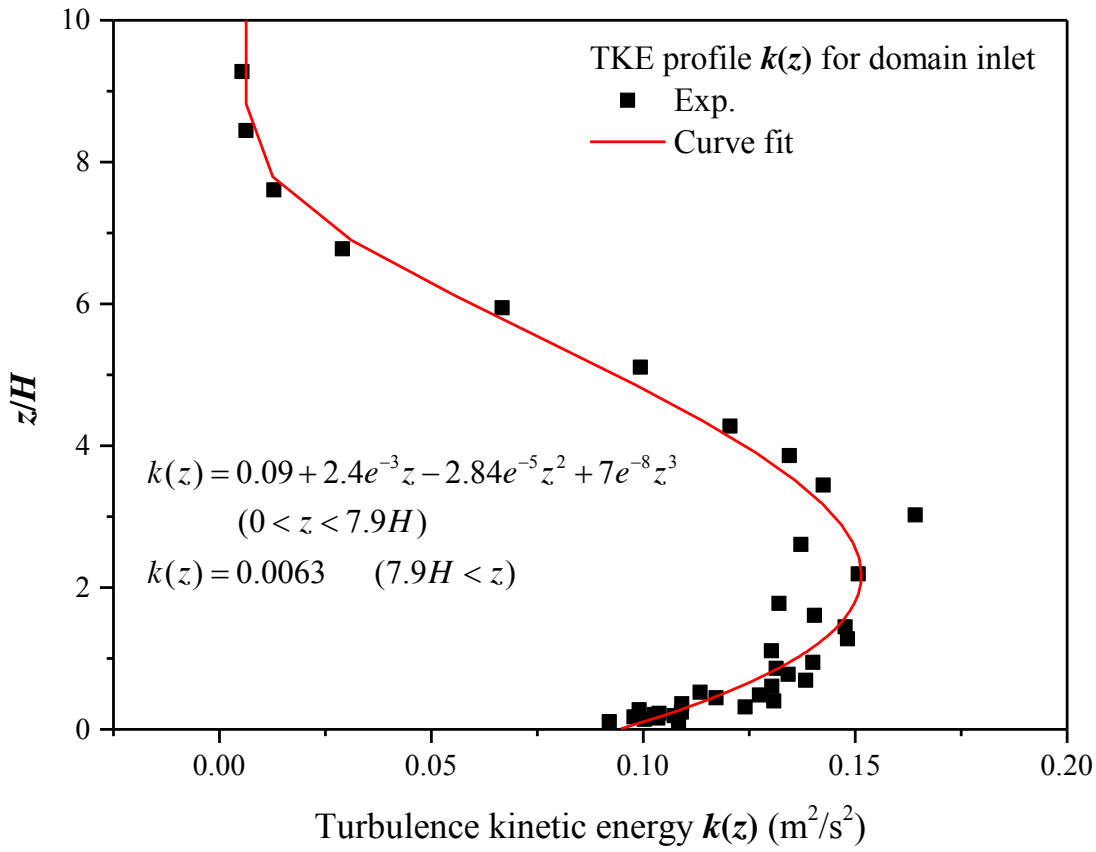
TKE profile k(z) for domain inlet
Exp.
Curve fit
$k(z) = 0.09 + 2.4e^{-3}z - 2.84e^{-5}z^2 + 7e^{-8}z^3$
$(0 < z < 7.9H)$
$k(z) = 0.0063 \quad (7.9H < z)$
z/H
Turbulence kinetic energy k(z) (m²/s²)

(d)

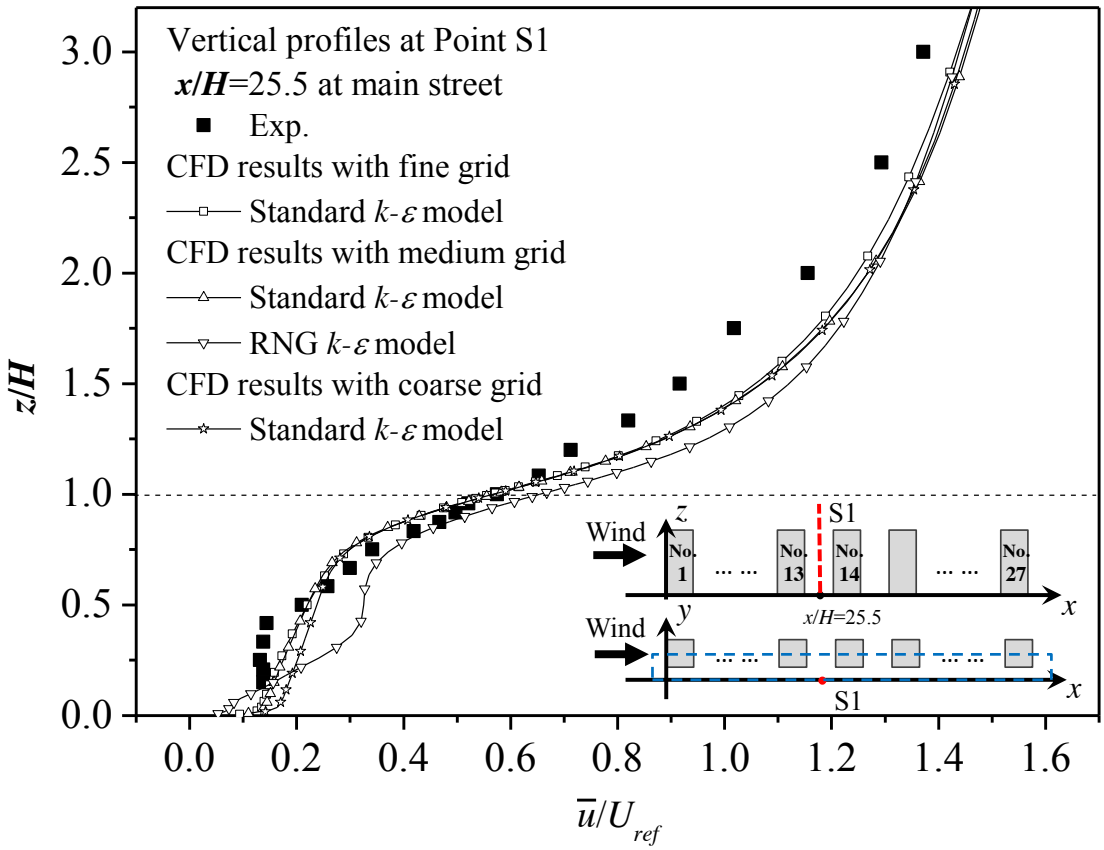
Vertical profiles at Point S1
x/H=25.5 at main street
Exp.
CFD results with fine grid
Standard k-ε model
CFD results with medium grid
Standard k-ε model
RNG k-ε model
CFD results with coarse grid
Standard k-ε model
Wind
No. 1
No. 13
No. 14
No. 27
S1
x/H=25.5
z/H
$\overline{u}/U_{ref}$

(e)

Fig. A1 (a) Overview of urban model studied in the wind tunnel laboratory at the University of Gavle; (b) Model configurations; (c) CFD computational domain; (d) $\overline{u}(z)$ and $k(z)$ profiles used for computational domain inlet; (e) Vertical profiles of normalized stream-wise velocity in CFD validation cases compared with wind tunnel measurement.

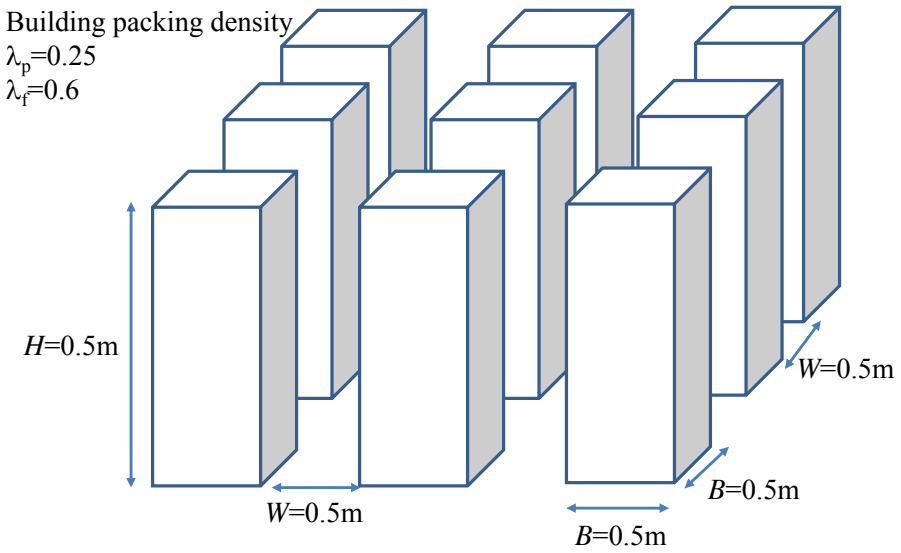

1137

1138 Fig.A2 Photos and model descriptions of 3D urban models in the scale-model outdoor

1139 field measurement of urban climate and health (SOMUCH) in suburb of Guangzhou,

1140 P.R. China.

1141